

Photoionization Suppression by Continuum Coherence: Experiment and Theory

L.P. Yatsenko *, T. Halfmann, B.W. Shore † and K. Bergmann
Fachbereich Physik der Universität, 67653 Kaiserslautern,

We present experimental and theoretical results of a detailed study of laser-induced continuum structures (LICS) in the photoionization continuum of helium out of the metastable state $2s\ ^1S_0$. The continuum dressing with a 1064 nm laser, couples the same region of the continuum to the $4s\ ^1S_0$ state. The experimental data, presented for a range of intensities, show pronounced ionization suppression (by as much as 70% with respect to the far-from-resonance value) as well as enhancement, in a Beutler-Fano resonance profile. This ionization suppression is a clear indication of population trapping mediated by coupling to a continuum. We present experimental results demonstrating the effect of pulse delay upon the LICS, and for the behavior of LICS for both weak and strong probe pulses. Simulations based upon numerical solution of the Schrödinger equation model the experimental results. The atomic parameters (Rabi frequencies and Stark shifts) are calculated using a simple model-potential method for the computation of the needed wavefunctions. The simulations of the LICS profiles are in excellent agreement with experiment. We also present an analytic formulation of pulsed LICS. We show that in the case of a probe pulse shorter than the dressing one the LICS profile is the convolution of the power spectra of the probe pulse with the usual Fano profile of stationary LICS. We discuss some consequences of deviation from steady-state theory.

PACS number(s): 42.50.Hz , 32.80.Fb, 32.80.Qk

arXiv:physics/9901017v1 [physics.atom-ph] 14 Jan 1999

*Permanent address : Institute of Physics, Ukrainian Academy of Sciences, prospekt Nauki 46, Kiev-22, 252650, Ukraine
†Permanent address: Lawrence Livermore National Laboratory, Livermore, CA 94550, USA

I. INTRODUCTION

A. Continuum coherence

The properties of the continuum of quantum states observed in the photoionization of an atom or the dissociation of a molecule have attracted interest since the first formulations of quantum theory. Until the widespread use of lasers, the continuum was regarded as a dissipative system, to be treated by means of rate equations (typically using the approximation of the Fermi Golden Rule [1] to calculate the transition rate into the continuum). Contemporary views no longer regard continuum states as an irreversible drain of probability. An electron acted upon by a laser field of sufficiently high frequency to produce ionization does not move irreversibly away from the binding region [2–4]. Laser interactions with a continuum have been shown to exhibit Rabi-type oscillations (if the laser field is sufficiently strong) [5,6] and to enable nearly complete population transfer into a continuum (i.e. photoionization or photodissociation [7]) or from a continuum (i.e. photorecombination [8]). Both theoretical [7,9–12] and experimental [6,13,14] work has shown that the wavefunction of an electron in a laser field may often maintain coherence during the course of photoionization, and that photodissociation can also maintain coherence. Consequences of continuum coherence are to be found in the well-studied phenomena of autoionization [15–17], which is revealed as a resonance in plots of photoionization cross-sections versus frequency. Such resonances display the effect of interference between two ionization channels whose destructive interference can lead to complete suppression of photoionization at a specific wavelength.

One of the more interesting coherent phenomena involving the continuum is the use of a laser field to embed an autoionization resonance into an otherwise featureless photoionization continuum. This dressing of a continuum by a bound state by means of a laser field is termed a “laser induced continuum structure” (LICS) [18–25].

As with other types of resonances described by scattering theory, LICS can be observed in various reaction channels. In the LICS observed in photoionization a strong laser field, connecting an unpopulated bound state to the continuum, mixes some bound-state character into the continuum; it places a resonance into the continuum. This optically induced resonance can be detected by a second (possibly weaker) laser field which serves as a probe and induces a transition from a populated bound state into the newly structured continuum.

We remark that when the continuum is composed of several channels (derived e.g. from different asymptotic internal states of dissociation products) the dissociation has been shown to give rise to a quantum control scheme [26] in which the ratio between the asymptotic channels can be controlled by tuning the dissociating (or dressing) laser across a LICS resonance.

Theoretical descriptions of continuum structure near autoionizing resonances have been presented [27–31] as have LICS in the absence of such resonances [32,33]. Observations of LICS in photoionization near autoionization resonances [13,14,34,35] as well as observations of LICS in photoionization to an otherwise *unstructured* continuum [18–25] have been reported recently. Under appropriate conditions this LICS can lead to the suppression of photoionization, by creating a coherent-superposition of bound states immune to photoionization (a trapped state, or dark state [36]). The occurrence of significant photoionization suppression signals the creation of a dark state; only with coherent excitation can this aspect of continuum coherence be revealed.

B. The resonance profile

When a coherent radiation field resonantly excites a two-state system, then a probing of either energy level by a weak probe field reveals a splitting (the Autler-Townes splitting) attributable to the dressing of bare atomic states by a strong field [37]. When the strong transition connects a bound (but unpopulated) state to a continuum, a weak probe will again reveal structure, the LICS.

The theoretical basis for describing LICS has been presented in numerous articles (see for example [38,39]), for cases in which the fields are constant-amplitude continuous-wave monochromatic, and for pulsed radiation. As such work has shown, the LICS of photoionization typically takes the form of an asymmetric window resonance, for which the frequency dependence of the photoionization cross-section $\sigma(\omega)$ may be parameterized by the form of a typical scattering resonance in a background [17,40]

$$\sigma(\omega) = C(\omega) + \frac{B + Ax}{x^2 + 1} \quad (1)$$

where $x \equiv (\omega - \omega_R)/(\Gamma/2)$ is a dimensionless detuning of the light frequency ω away from the resonance value ω_R , measured in units of the resonance-width parameter (or loss rate) Γ . Equivalently, one may use a form akin to that

developed by Fano [15] and Fano and Cooper [16] to describe the Beutler-Fano profiles observed in autoionization or electron-scattering cross-sections,

$$\sigma(\omega) = \sigma_b(\omega) + \sigma_a \frac{(x + q)^2}{x^2 + 1} \quad (2)$$

where q is the dimensionless Fano q parameter. The terms $C(\omega)$ or $\sigma_b(\omega)$ are slowly varying (or constant) contributions to the cross section. Appendix A describes simple estimators of the parameters when fitting experimental data to this functional form.

We found it useful to use a variant of these parameterizations,

$$\sigma(D) = \sigma_a \text{Re} \left[1 - \frac{(1 - iq)^2 \Gamma_d}{\Gamma_d + \Gamma_0 - i2(D - D_0)} \right] \quad (3)$$

where D is the detuning of the probe laser, and Γ_d and Γ_0 are parameters discussed in section II C.

Although we have presented profile formulas appropriate to photoionization cross-sections, what is important for the present paper is the functional dependence of an experimentally observed quantity, here $\sigma(\omega)$, upon a dimensionless detuning variable x . It often proves convenient to fit dimensionless observables with these parameterizations, in which case the parameters A , B and C , or σ_a and σ_b , become dimensionless.

C. Present work

In an earlier paper [25] we presented experimental evidence for substantial suppression of photoionization by means of LICS. As we stressed, only with the use of very coherent laser pulses, together with an appropriate choice of atomic states, is it possible to observe pronounced suppression. Here we present further experimental results showing dependence of the LICS profile on various pulse properties.

Our experimental results are for LICS induced in metastable helium, by means of a dressing laser (1064 nm) that couples the $4s \ ^1S_0$ state into a continuum. The structure is observed by scanning the frequency of a probe laser which, at a wavelength of 294 nm, couples the $2s \ ^1S_0$ state into this same continuum. Figure 1 shows the relevant energy levels and transitions.

We discuss numerical simulation of the experimental results, and show that with calculations of atomic parameters the observations are in excellent agreement with computations. We present an analytic description of pulsed LICS, emphasizing the difference between pulsed and steady excitation. These results reduce to expressions (1) and (2) under appropriate conditions. Our calculations of needed atomic parameters (polarizabilities, Stark shifts, etc.) are done using a simple effective-potential model of the active electron (see Appendix B). We describe this method, and we show that this model provides quantitative agreement with experiments.

II. EXPERIMENTAL

Our observations of LICS in the photoionization of helium are carried out using an atomic beam of metastable helium atoms, which cross spatially overlapping beams of pulsed laser radiation. We control the duration of the pulses and the overlap in space and time. Figure 2 shows a schematic diagram of the experimental apparatus.

A. The apparatus

a. The atomic beam. A pulsed beam of metastable helium atoms is formed as helium, at a stagnation pressure of 1200 mbar, expands through a nozzle (General Valve, opening diameter 0.8 mm) and enters a region of pulsed discharge located 4 mm from the nozzle. A skimmer (diameter 0.8 mm) placed 40 mm from the nozzle collimates the atomic beam and separates the source chamber from the region of interaction and detection.

b. The metastable atoms. The metastable states of helium used for our photoionization experiments are populated in a gas discharge, where the atoms are excited from the ground state $1s\ ^1S_0$ by pulsed electron impact. To enhance efficiency and stability of the discharge, a filament, placed 10 mm downstream, provides the discharge with a continuous electron current of several mA. The peak current, produced by ions and electrons in the pulsed discharge, reaches 20 mA. The electron source enhances the efficiency of the metastable production by at least two orders of magnitude and the breakdown voltage is reduced to 1/50 of the value needed for an unseeded discharge.

c. Diagnostics of metastable population We deduce the population of metastable atoms by using a two-photon version of REMPI (resonant-enhanced multiphoton ionization) to produce photoions, with pulsed radiation from a broadband dye laser (LPD 3000, Lambda Physik). The ions are observed as an electric current. Figure 3 shows the REMPI transitions used to detect the $2s\ ^1S_0$ and $2s\ ^3S_1$ metastable atoms.

Figure 4 shows the ionization signal of the metastable singlet and triplet states as a function of probe-laser wavelength. The REMPI transitions are strongly broadened by saturation. We also confirmed that the ionization is saturated. Populations are inferred from the heights of the ionization signal peaks. Typically 90% of the metastable population is found in the triplet state $2s\ ^3S_1$, and 10% is found in the singlet state $2s\ ^1S_0$.

d. The lasers. The pulsed atomic beam crosses the coinciding axes of two pulsed laser beams: a UV probe pulse and an IR dressing pulse. The probe laser field, coupling the metastable state $2s\ ^1S_0$ to the ionization continuum (see Fig. 1), is derived from a single mode cw dye laser system operating at 587 nm. This radiation is amplified in a pulsed dye amplifier, pumped by the second harmonic of an injection-seeded Nd:YAG laser. The wavelength of the cw radiation is measured to an accuracy of $\Delta\lambda/\lambda = 2 \times 10^{-6}$ in a Michelson-type wavemeter, using a He-Ne laser, stabilized on an iodine line, as a reference. The pulsed radiation is frequency-doubled in a BBO crystal, thereby providing (probe) laser pulses with a pulse width $\Delta\tau = 2.3$ ns (half-width at $1/e$ of $I(t)$) at $\lambda = 294$ nm.

The pulse of the dressing laser couples the state $4s\ ^1S_0$ to the ionization continuum and induces the continuum structure. This pulse, obtained from the fundamental frequency of the Nd:YAG laser ($\lambda = 1064$ nm), has a pulse width $\Delta\tau = 5.1$ ns.

A folded optical delay line is used to adjust the time delay between the dressing and probe pulses. After passing through the optical setup, pulse energies of up to 2 mJ for the probe laser and up to 250 mJ for the dressing laser are delivered to the atomic beam. The laser diameters at the atomic beam position are 0.5 mm for the probe and 3.5 mm for the dressing laser, yielding peak intensities of up to $I_p^{(0)} = 100$ MW/cm² and $I_d^{(0)} = 300$ MW/cm², respectively. (we use a superscript $I^{(0)}$ to denote the peak value of a time-varying pulse $I(t)$.) Because of the large diameter of the dressing-laser beam, the variation of its intensity across the probe laser profile is small.

e. Ionization detection. Ionized helium atoms are mass-selectively detected with a double-thickness micro-sphere plate (El Mul Technologies) after passing through a 30 cm time-of-flight segment. The output current of the micro-sphere plate is amplified with fast broadband amplifiers and integrated in a boxcar gated integrator (EG & G 4121 B).

B. Results

The continuum structure induced by the dressing laser is revealed in the ionization of the metastable state $2s\ ^1S_0$ produced by the probe laser. When the probe laser is tuned across the two-photon resonance between the states $2s\ ^1S_0$ and $4s\ ^1S_0$, we observe a strong and spectrally narrow feature in the ionization cross-section (see the following subsections). The structure is due to the laser-induced mixing of the bound state $4s\ ^1S_0$ with the ionization continuum.

1. Background signal

At high laser intensities, two-photon ionization of the metastable triplet state (see Fig. 1) forms a background, which has to be subtracted from the total ion signal. The background ionization was determined by tuning the UV laser away from the region where LICS is observed and measuring the ionization probability with and without the IR laser present. The difference of these two currents (the difference signal) is attributed to the two-photon (IR + UV) ionization of the triplet level, the population of which exceeds that of the singlet level by about an order of magnitude.

Figure 5 shows the measured difference signal, relative to the total ion signal, as a function of probe intensity. The probe laser frequency is here tuned also far away from the two photon resonance between states $2s\ ^1S_0$ and $4s\ ^1S_0$. The plotted signal is proportional to the ionization probability of the $2s\ ^3S_1$ state. For comparison we show the calculated ionization probability for $2s\ ^3S_1$ state caused by one photon at 294 nm and one photon at 1064 nm, using the theoretical ionization probability. Using wavefunctions described in Appendix B we obtained the result $\Gamma_{triplet} = 1.6 \times 10^{-9} I_p I_d$. Here and elsewhere laser intensities are expressed in W/cm^2 and the unit for the rate is s^{-1} . The calculated relative transition probability is in good agreement with the experimental data.

From Fig. 5 we see that the background signal contributes only a few percent to the total ion signal for $I_p^{(0)} < 10\ \text{MW}/\text{cm}^2$, while it adds more than 30% for the highest probe laser intensity used here. This background signal has been subtracted for all the data presented below.

2. LICS for weak probe laser

If the probe laser is weak, the shape of the continuum structure is dominated by the strong dressing laser, and the probe does not affect the internal structure of the atom. It is therefore possible to distinguish between the influence of the dressing and probing lasers.

Figure 6 shows, for a weak probe laser, the observed structure in the ionization continuum of helium for various dressing-laser intensities (in each column) and for two pulse timings (in each row). The left-hand column of frames show the LICS produced by coincident laser pulses; the right-hand frames show LICS produced when the dressing pulse precedes the probe pulse (negative delay) by 5 ns. The dotted lines are results from numerical simulations, discussed in section III.

The continuum resonances exhibit typical asymmetric window-resonance structure as a function of frequency, such as are observed in autoionization. The LICS exhibit an enhancement of photoionization, taking largest value P_{max} at frequency ν_{max} , and a suppression of photoionization, a dip to P_{min} centered at frequency ν_{min} .

As can be seen, it is possible to control the photoionization probability by appropriately tuning the wavelength of the probe laser, thereby selecting the region of enhancement or suppression of ionization. Photoionization suppression indicates population trapping. We observe photoionization suppression as strong as a drop to 30% of the value far from resonance [25].

The primary effects of an increase in dressing-laser power are a broadening and a shift of the LICS profile, both for coincident and delayed laser pulses. This is expected: the dressing laser intensity is responsible for the width-parameter Γ and the Stark shifts.

For delayed laser pulses the LICS is not as strong as, and is spectrally narrower than, for coincident pulses. This is because when pulses are not coincident, the dressing laser intensity is lower when the probe pulse samples the continuum structure: the LICS width is smaller and less pronounced when the dressing is weaker.

3. LICS for strong probe laser

For a strong probe laser, it is no longer possible to distinguish between the effect of the dressing and probing laser pulses. Both pulses contribute to the continuum structure. Whether the influence of the probe pulse is negligible or not can be estimated from the ionization probability of state $2s\ ^1S_0$. Figure 7 shows the measured ionization probability of state $2s\ ^1S_0$ as a function of the probe laser intensity (in the absence of the dressing laser). The observed dependence is in good agreement with the theoretical prediction (Fig. 7, dashed curve), based on the calculated ionization rate $\Gamma_{2s,p}$ (see Table II).

For probe intensities of several tens of MW/cm^2 the ionization is strongly saturated. In this regime the interaction induced by the probe laser cannot be considered as a small perturbation of the atomic structure. The observed profile will consequently deviate from the profiles of eqns. (1) and (2).

Figure 8 compares the observed LICS for weak and strong probe pulses. The peak values of probe laser intensities are $I_p^{(0)} = 0.5 \text{ MW/cm}^2$ (Fig. 8a) and $I_p^{(0)} = 40 \text{ MW/cm}^2$ (Fig. 8b). The peak intensity of the dressing laser was $I_d^{(0)} = 44 \text{ MW/cm}^2$ and 50 MW/cm^2 . An increase of the probe laser intensity reduces the peak value of the ionization, relative to the value far from resonance, from 140% to 110%. This reduction of the photoionization enhancement is the result of saturation: the atoms are rapidly photoionized for all frequencies except those where photoionization is suppressed. Because the strong probe pulse ionizes about 90% of the population of the metastable singlet state (see Fig. 7), the maximum enhancement of the ionization probability can be no more than 10%.

C. Fitting Experimental Data

To parameterize our experimental results we first subtracted a linearly varying background fitted to the far-from-resonance values, and then performed a least-squares fit of the resulting data to a version of the Breit-Wigner or Fano-Cooper formula, Eqn. (3). This parameterization introduces two contributions to the overall width parameter $\Gamma = \Gamma_d + \Gamma_0$. The ionization rate of the dressing laser, Γ_d , can, in principle, be computed using the traditional Fermi Golden Rule. The remaining term, Γ_0 , represents an additional empirical rate; it expresses the effect of spontaneous emission, of fluctuations of intensity or phase, and other stochastic processes. Figure 9 shows an example of the experimental data (small squares) and the best analytic fit to this curve (dashed line). As can be seen, the data is very well described by the analytic expression. Table I presents values of the least squares parameters for undelayed pulses.

TABLE I. Fits of the experiment, $\Delta t = 0$

$I_p^{(0)}$	$I_d^{(0)}$	q	Γ	Γ_0	Γ_d	Γ_{theory}
2.5	38	0.66	0.83	0.29	0.54	0.45
4	75	0.71	1.36	0.42	0.94	0.88
4	140	0.67	2.21	0.61	1.61	1.64

Here $I_p^{(0)}$ and $I_d^{(0)}$ are the peak intensities of the probe and dressing lasers in MW/cm^2 , q is the Fano q parameter, Γ_d is the ionization rate from the dressing laser, Γ is the overall width parameter, $\Gamma_0 = \Gamma - \Gamma_d$, and Γ_{theory} is the theoretical value for Γ_d . All rates are in units of GHz.

From several such fits we found the trend of the width parameters as a function of dressing intensity. Figure 10 plots values of the parameter Γ_0 and of the empirically determined Γ_d . We show also the theoretical value Γ_{theory} of the photoionization rate Γ_d , calculated using the method described in section B. Theory and experiment are in very good agreement.

Laser intensity fluctuations lead to fluctuations in the laser-induced Stark shifts. These fluctuations give an additional contribution to the LICS width,

$$\Gamma_0^{Stark} = \langle S_{4s,d}^0 - S_{2s,d}^0 \rangle_{Fluc} \quad (4)$$

Here $S_{i,j}^0$ is the peak Stark shifts of state i induced by laser field j (see Section III). With $I_d^{(0)} = 75 \text{ MW/cm}^2$ and typical laser intensity fluctuations of $\Delta I_d^{(0)} = \pm 10 \% I_d$ the additional broadening is $\Gamma_0^{Stark}/2\pi = 0.2 \text{ GHz}$.

III. NUMERICAL SIMULATION

Usually laser induced continuum structures are deduced from the equations for the density matrix of an atom. This approach allows one to take into account coherence dephasing processes such as laser frequency fluctuations, collisions etc. But in the case of coherent laser pulses, with transform-limited bandwidths, one can significantly simplify the description of the process by using the time-dependent Schrödinger equation for the amplitudes of atomic states involved in the process.

A. The main equations

We consider an atom interacting with two laser fields: a probe laser with amplitude $\mathcal{E}_p(t)$, intensity $I_p(t)$ and carrier frequency ω_p , and a dressing laser with amplitude $\mathcal{E}_d(t)$, intensity $I_d(t)$ and carrier frequency ω_d . The total electric field is

$$\mathbf{E}(t) = \text{Re} \sum_{j=p,d} \mathbf{e}_j \mathcal{E}_j(t) \exp(-i\omega_j t), \quad (5)$$

where \mathbf{e}_j is a unit vector. The probe and dressing lasers are tuned close to the two-photon Raman resonance between states 1 and 2, and their carrier frequencies differ from exact resonance by the two-photon detuning D , given by

$$\hbar D \equiv \hbar(\omega_p - \omega_d) - (E_2 - E_1). \quad (6)$$

We express the state vector $|\Psi(t)\rangle$ of the atom as a combination of two particular discrete states 1 and 2, with energies E_1 and E_2 , together with a sum over all other bound states and an integral over continuum states:

$$|\Psi(t)\rangle = \sum_{n=1,2} C_n(t) \exp(-iE_n t/\hbar) |n\rangle \quad (7)$$

$$+ \sum_{n \neq 1,2} A_n(t) \exp(-iE_n t/\hbar) |n\rangle \quad (8)$$

$$+ \sum_j \int dE A_{E,j}(t) \exp(-iEt/\hbar) |E, j\rangle, \quad (9)$$

where $|E, j\rangle$ is the continuum state with energy E (quantum number j identifies different possible continua).

As is customary [9,12,37,39,41–43] we adiabatically eliminate all amplitudes except those of states 1 and 2. In so doing, we obtain effective interactions, and dynamic energy shifts, expressible in terms of a polarizability tensor [37],

$$\mathbf{Q}_{mn}(\omega) = \sum_k \frac{\langle m|\mathbf{d}|k\rangle \langle k|\mathbf{d}|n\rangle}{E_k - E_m - \hbar\omega} + \int dE \sum_j \frac{\langle m|\mathbf{d}|E, j\rangle \langle E, j|\mathbf{d}|n\rangle}{E - E_m - \hbar\omega}, \quad (10)$$

where \mathbf{d} is the dipole-moment operator. The continuum integral includes the resonance energy $E = E_m + \hbar\omega$, which is dealt with by breaking the integration into a nonsingular principal value part (denoted by \mathcal{P}) and a resonant part (yielding the transition rate of a Fermi Golden Rule),

$$\begin{aligned} \text{Re}\mathbf{Q}_{mn}(\omega) &= \mathcal{P} \sum_k \frac{\langle m|\mathbf{d}|k\rangle \langle k|\mathbf{d}|n\rangle}{E_k - E_m - \hbar\omega} + \int dE \sum_j \frac{\langle m|\mathbf{d}|E, j\rangle \langle E, j|\mathbf{d}|n\rangle}{E - E_m - \hbar\omega}, \\ \text{Im}\mathbf{Q}_{mn}(\omega) &= \sum_j \pi \langle m|\mathbf{d}|E = E_m + \hbar\omega, j\rangle \langle E = E_m + \hbar\omega, j|\mathbf{d}|n\rangle. \end{aligned} \quad (11)$$

The adiabatic elimination yields a two-state time-evolution equation, which may be written [39]

$$i \frac{d}{dt} \begin{bmatrix} C_1(t) \\ C_2(t) \end{bmatrix} = \frac{1}{2} \begin{bmatrix} 2S_1(t) - i\Gamma_1(t) - i\gamma_1 & -(i+q)\Omega(t) \\ -(i+q)\Omega(t) & 2S_2(t) - i\Gamma_2(t) - i\gamma_2 - 2D \end{bmatrix} \begin{bmatrix} C_1(t) \\ C_2(t) \end{bmatrix}. \quad (12)$$

This equation, the basis for our simulation, requires dynamic Stark shifts $S_i(t)$, detuning D , photoionization rates $\Gamma_i(t)$, spontaneous emission rates γ_i , an effective Rabi frequency $\Omega(t)$, defined below in Eqn. (17), and the Fano

parameter q . These various parameters can be obtained from atomic wavefunctions, as the following paragraphs show.

We are interested in the total ionization probability after pulses cease, P . This can be determined if we know the populations of states 1 and 2 after the action of the laser pulses:

$$P = 1 - |C_1(\infty)|^2 - |C_2(\infty)|^2. \quad (13)$$

The LICS profile is taken as the variation of P with two-photon detuning D .

B. Formulas for Atomic Parameters

The theoretical ionization rates and Stark shifts are obtainable by summing partial rates:

$$\Gamma_i(t) = \sum_{j,\alpha} \Gamma_{i\alpha}^{(j)}(t), \quad S_i(t) = \sum_{\alpha} S_{i\alpha}(t), \quad (14)$$

where $\Gamma_{i\alpha}^{(j)}(t)$ is the ionization rate from state i to continuum j caused by probe ($\alpha = p$) or dressing ($\alpha = d$) lasers

$$\Gamma_{i\alpha}^{(j)}(t) = \frac{\pi}{2\hbar} |\mathcal{E}_\alpha(t)|^2 |\langle i | \mathbf{e}_\alpha \cdot \mathbf{d} | E = \hbar\omega_\alpha - E_i, j \rangle|^2, \quad (15)$$

and $\hbar S_{i\alpha}(t)$ is the dynamic Stark shift of the energy of state i produced by laser α :

$$S_{i\alpha}(t) = -\frac{1}{4\hbar} |\mathcal{E}_\alpha(t)|^2 \mathbf{e}_\alpha \cdot [\mathbf{Q}_{ii}(\omega_\alpha) + \mathbf{Q}_{ii}(-\omega_\alpha)] \cdot \mathbf{e}_\alpha^*. \quad (16)$$

The quantity

$$\Omega(t) = \sum_j \sqrt{\Gamma_{1p}^{(j)}(t) \Gamma_{2d}^{(j)}(t)} \quad (17)$$

is an effective Rabi frequency for the two-step transition from the state 1 to the state 2 with intermediate population of the continuum states j with energy $E \simeq \hbar\omega_p - E_2 + E_1 \simeq \hbar\omega_d - E_1 + E_2$. The Fano q parameter can be evaluated from the expression [12,39,42,43]

$$q\Omega(t) = \frac{1}{2\hbar} |\mathcal{E}_p(t)\mathcal{E}_d(t)| \mathbf{e}_p \cdot [\mathbf{Q}_{12}(\omega_p) + \mathbf{Q}_{12}(-\omega_d)] \cdot \mathbf{e}_d^*. \quad (18)$$

From Eqns. (17) and (18) it is apparent that q depends only on atomic properties.

In principle, all of these quantities can be calculated if the atomic wavefunctions are known.

We note that the Fano parameter q is basically the ratio of polarizability (such as occurs in a Raman transition) to the product of two dipole transition moments into the continuum. In systems with $|q| \gg 1$ the Raman-type transitions dominate. The ionization probability is enhanced, when tuning the probe laser across the two-photon resonance, because Raman-type transitions open additional (multiphoton) ionization channels from the initial state to the ionization continuum. If $q = 0$ no Raman-type transitions are present and no enhancement of ionization can be observed.

C. Values for Atomic Parameters

For the calculations we need the values of many transition matrix elements, both bound-bound and bound-continuum. Due to the relative simplicity of the two-electron helium atom there exist several methods, of varying complexity and accuracy, which can provide the needed wavefunctions [44–48]. However, these methods are usually optimized for the calculation of particular parameters (such as the ionization energy).

Therefore, for our purposes it is desirable to use some simpler method. The simplest of these are based on the assumption that each electron moves in an effective central potential, and that therefore the atomic wavefunction is separable into a product (antisymmetrized) of individual electron orbitals, each of which has a spherical harmonic for

angular dependence and a radial dependence given by the solution to an ordinary differential equation (see Appendix B).

We have found that a simple single-electron model potential satisfies requirements for speed and accuracy. Appendix B describes the mathematics of this method for computing matrix elements. As noted there, a single empirically determined parameter λ_ℓ fixes the potential, and hence all the wavefunctions, for each orbital angular momentum ℓ .

Table II presents the theoretical values we used in the simulation.

TABLE II. Theoretical values for simulation

q	0.73		
Γ_{1p}	$13.4 \times I_p$	S_{1p}	$9.0 \times I_p$
Γ_{2p}	$1.9 \times I_p$	S_{2p}	$13.0 \times I_p$
Γ_{1d}	0	S_{1d}	$70.0 \times I_d$
Γ_{2d}	$73.7 \times I_d$	S_{2d}	$142.0 \times I_d$

Here I_p and I_d are the intensity of probe and dressing lasers expressed in W/cm^2 . The ionization rates and Stark shifts are expressed in s^{-1} . These results are in good agreement with more elaborate computations carried out by Klystra, Paspalakis and Knight [49]. The agreement with these more accurate results, and the successful fitting of our experimental data, support the validity of our atomic wavefunctions.

The numerical simulation of the observed LICS-profile includes experimentally determined intensity fluctuations and integration over the spatial probe laser intensity profile. These effects have to be taken into account, because position, bandwidth and shape of the LICS are strongly dependent on the laser power.

To account for pulse-to-pulse variations of the intensity we average our computed ionization probabilities over a distribution of peak pulse intensities. We used a Monte-Carlo method to estimate the relevant integrals, assuming intensities evenly distributed between $0.9 I_p$ and $1.1 I_p$. The results of the simulations are in excellent agreement with the experimental results, as are seen in Fig. 6.

D. Deviations from Steady State

When the probe pulse is weak, and much shorter than the strong dressing pulse, the excitation can be regarded, to a first approximation, as an example of steady-state LICS (see sections IV D - IV F). One expects, under these circumstances, that an observed LICS profile will follow the form of Eqns. (1) or (2) [39] or, equivalently (3), and that the parameters q_{fit} and Γ_{fit} obtained from fitting such an expression will be equal to the values q_{theo} and Γ_{theo} obtained by evaluating matrix elements.

To show the effects of pulse shapes we display, in Fig. 11 the profiles predicted in two approximations:

- Steady-state profile, using the theoretical q value.
- Simulation for a single pair of pulses (i.e. transient theory), again using the theoretical q value.

The difference between these curves is small but it shows the importance of transient effects and the limitation of the steady-state approximation of sections IV D - IV F. Here “transient” means that we determine the ionization probability from the solution of the differential equations (12) thereby taking into account the pulsed variability of the probe interaction. The spectral width of this pulse, approximately $1/\tau_p$, effectively contributes additional broadening, Γ_0 , to the LICS profile. Only with the steady-state approximation ($\tau_p \rightarrow \infty$ and $\Gamma_0 = 0$) is there complete suppression of photoionization.

E. Delayed Pulses

In addition to the results just described, for which the probe pulse was timed to coincide with the peak value of the dressing pulse, we have also obtained results with probe pulses delayed with respect to the peak of the dressing pulse. As with the previously discussed results, it is possible to fit these LICS profiles with the function shown in Eqn. (3). Table III E gives the values of parameters from these fits.

TABLE III. Fits of experiment, $\Delta t = -5$ ns

$I_p^{(0)}$	$I_d^{(0)}$	q	Γ	Γ_0	Γ_d	$I_d^{(eff.)}$
2.5	38	0.63	0.66	0.32	0.34	29
4	75	0.67	0.97	0.42	0.55	47
4	140	0.67	1.72	0.57	1.15	98

The width parameters obtained from fits for delayed pulses are significantly larger than what one would expect from the value of the dressing intensity at the peak of the probe pulse. To emphasize this point, Fig. 12 shows the dressing and probe envelopes. The point marked B indicates the dressing intensity required to produce the observed width. The point marked A shows the (lower) intensity occurring at the peak of the probe pulse. As these points show, it is not possible to evaluate the LICS profile by considering only the moment of peak probe intensity. The observed profile averages in time the Stark shifts and the ionization rates.

F. Summary

In the simulations of the experimental data presented above, intensity fluctuations of both lasers as well as an integration over the spatial probe laser profile are taken into account to describe the observed LICS. In the present experiments the diameter of the dressing laser was much larger than that of the probe laser, and so the spatial variation of the dressing laser intensity was neglected in the simulation.

a. Weak probe When the probe laser is weak, the continuum resonance is mainly determined by properties of the dressing laser. Fluctuations in the dressing laser intensity can disturb the observation of the continuum resonance. A change in the dressing laser intensity changes the Stark shifts as well as the peak value and central wavelength of the LICS. Because the Stark shifts follow the fluctuations of the dressing laser intensity, the position of the structure varies with every laser pulse. The observed LICS is therefore broadened by the fluctuations. In the most extreme cases the detected ion signal, for a fixed detuning, fluctuates between the maximum ionization enhancement and the ionization suppression. The averaging produced by the fluctuation reduces the LICS contrast between maximum enhancement and minimum suppression.

A weak probe laser does not affect the LICS, and so the probe laser intensity fluctuations have no influence on the continuum resonance if there are no dramatic variations in the laser intensity for single pulses. It is not necessary, in simulations, to average over intensity fluctuations of a weak probe laser.

b. Strong probe When the probe laser is strong the continuum is modified by the dressing laser *and* by the probe laser. The influence of the strong probe laser can be observed in the saturation of ionization, i.e. a reduced enhancement in the continuum resonance. Although saturation might be reached in the center of the spatial probe laser profile, the intensity could still be below saturation in the wings. The maximum enhancement is stronger in the wings than in the center of the profile. An integration over the spatial profile of a strong probe laser therefore leads to less saturation than expected for constant strong laser intensity.

Fluctuations in the probe laser intensity determine, as do fluctuations in the dressing laser intensity, additional Stark shifts, i.e. variations in linewidth and position of the continuum resonance, as discussed above.

IV. ANALYTICAL EXPRESSIONS FOR THE LICS PROFILE

It is always instructive to augment numerical simulation with analyses that can provide explicit formulas for various observables. We present in the following sections some examples of such formulas. We consider pulsed excitation, so that one cannot always rely on the stationary solutions that are known to give the formulas Eqn. (1) and Eqn. (2) for the LICS shape.

A. General theory

If we neglect the coupling $\Omega(t)$ of Eqn. (12), then the amplitude of $C_1(t)$ decays exponentially with time, while its phase depends on the Stark shift $S_1(t)$. With this in mind we introduce the new variables

$$h_1(t) = \ln C_1(t) - i \int_{-\infty}^t dt' S_1(t'), \quad (19)$$

$$h_2(t) = C_2(t)/C_1(t) \quad (20)$$

In terms of the new variables the populations of states 1 and 2 after the interaction with the laser pulses are

$$|C_1(t)|^2 = \exp[2\text{Re}h_1(t)] \quad \text{and} \quad |C_2(t)|^2 = \exp[2\text{Re}h_1(t)] |h_2(t)|^2. \quad (21)$$

In the following we assume the probe pulse $\mathcal{E}_p(t)$ to be weak, meaning that for the pulse duration τ_p the direct ionization probability

$$\varepsilon^2 \equiv \int_{-\infty}^{\infty} dt \sum_j \Gamma_{1p}^{(j)}(t) \quad (22)$$

remains small: $\varepsilon^2 \ll 1$. We therefore seek solutions in the form of a power series in the parameter ε . Because for $\varepsilon = 0$ the populations are $|C_1(t)|^2 = 1$ and $|C_2(t)|^2 = 0$, the variables $h_i(t)$ vanish for $\varepsilon = 0$ and the series expansion reads

$$h_i(t) = \sum_k \varepsilon^k h_i^{(k)}(t).$$

We assume that the state 1 is long lived so that one can neglect the spontaneous decay during the interaction with the laser pulses ($\gamma_1 = 0$). We assume also that the frequency ω_2 is small enough that the dressing field does not ionize the atom in state 1, and hence $\Gamma_1(t) = \sum_j \Gamma_{1p}^{(j)}(t)$. The equations for $h_1(t)$ and $h_2(t)$ derived from Eqn. (12) then read

$$\frac{d}{dt} h_1(t) = -\frac{\Gamma_1(t)}{2} + \frac{(iq-1)}{2} \Omega(t) h_2(t), \quad (23)$$

$$\frac{d}{dt} h_2(t) = -\left(\frac{\Gamma_2(t)}{2} + \frac{\gamma_2}{2} - \frac{\Gamma_{1p}(t)}{2} - iD_{eff}(t) \right) h_2(t) + \frac{(iq-1)}{2} \Omega(t) (1 - h_2(t)^2), \quad (24)$$

where $D_{eff}(t) = D - S_2(t) + S_1(t)$ is the two-photon detuning incorporating the Stark-shifted resonance. We require solutions that vanish initially: $h_1(-\infty) = h_2(-\infty) = 0$.

The value of $h_1(t)$ obtained from Eqn. (23), when integrated over the pulse duration τ_p , is proportional to ε^2 . To first order in ε Eqn. (24) reads

$$\frac{d}{dt} h_2^{(1)}(t) = -\left(\frac{\Gamma_2(t)}{2} + \frac{\gamma_2}{2} - iD_{eff}(t) \right) h_2^{(1)}(t) + \frac{(iq-1)}{2} \Omega(t). \quad (25)$$

The solution of this equation with the initial condition $h_2(-\infty) = 0$ is

$$h_2^{(1)}(t) = \frac{(iq-1)}{2} \int_0^\infty d\tau \Omega(t-\tau) \exp \left[-\int_{t-\tau}^t dt' \left(\frac{\Gamma_2(t')}{2} + \frac{\gamma_2}{2} - iD_{eff}(t') \right) \right]. \quad (26)$$

Using Eqns. (26) and (23) we find $h_1^{(2)}(t)$ in second order of perturbation theory to be:

$$h_1^{(2)}(t) = -\int_{-\infty}^t \frac{\Gamma_1(t')}{2} dt' + \frac{(iq-1)}{4} \int_{-\infty}^t \Omega(t') h_2^{(1)}(t') dt'. \quad (27)$$

From (26) one can see that $h_2^{(1)}(+\infty) = 0$ and hence, to second order in the small parameter ε , the ionization probability P is

$$P = 1 - \exp(-\kappa), \quad (28)$$

where the exponent κ is the value of the variable $h_1(t)$ in the limit of long times,

$$\kappa = -2\text{Re} \left[h_1^{(2)}(+\infty) \right].$$

Using Eqn. (27) for $h_1^{(2)}(t)$ and Eqn. (26) for $h_2^{(1)}(t)$ we can write the parameter κ as

$$\kappa = \kappa_0 - \text{Re} \left\{ \frac{(iq-1)^2}{2} \int_{-\infty}^{+\infty} dt \int_0^{\infty} d\tau \Omega(t) \Omega(t-\tau) \exp[-\varphi(t, \tau)] \right\}, \quad (29)$$

where κ_0 is the value of the parameter κ in the absence of the dressing laser,

$$\kappa_0 \equiv \int_{-\infty}^{+\infty} \Gamma_1(t) dt, \quad (30)$$

and $\varphi(t, \tau)$ is

$$\varphi(t, \tau) \equiv \int_{t-\tau}^t dt' \left(\frac{\Gamma_2(t')}{2} + \frac{\gamma_2}{2} - iD_{eff}(t') \right). \quad (31)$$

Equations (28) and (29) include explicitly the time dependence of the effective two-photon detuning, and thus they provide the desired analytic formulas for the LICS profile. This expression will be simplified below for some interesting limiting cases.

For small values of κ the ionization probability, and hence the observed LICS profile, is proportional to κ ,

$$P \approx \kappa \quad \text{for } \kappa \ll 1.$$

In this approximation κ provides a theoretical estimate of the observed LICS profile of P ; conversely, a parametric fit of the detuning dependence of the observed P can be interpreted as the detuning dependence of κ .

B. Short probe pulse

Maintaining the assumption of a weak probe pulse, $I_p^{(0)} \ll I_d^{(0)}$, we now consider laser pulses of different durations, and take the probe pulse duration τ_p to be much shorter than the duration τ_d of the dressing pulse ($\tau_p \ll \tau_d$). In this case the main contribution to the integrals over τ and t in Eqn. (29) stems from $\tau \leq \tau_p$ and $|t| \leq \tau_p$. Hence we can write the phase factor of Eqn. (31) in the form

$$\varphi(t, \tau) = \left[\frac{\Gamma_2(t_m)}{2} + \frac{\gamma_2}{2} - i\Delta \right] \tau, \quad (32)$$

where t_m is the time when the intensity of the probe pulse reaches the maximum and $\Delta \equiv D_{eff}(t_m)$ is the effective two-photon detuning at the moment of peak pulse. Using the Fourier expansion of the two-photon Rabi frequency $\Omega(t)$

$$\tilde{\Omega}(\omega) = \frac{1}{2\pi} \int_{-\infty}^{+\infty} d\omega \exp(i\omega t) \Omega(t)$$

we rewrite Eqn. (29) as

$$\kappa = \kappa_0 - \pi \text{Re} \left\{ (iq-1)^2 \int_{-\infty}^{+\infty} d\omega \frac{|\tilde{\Omega}(\omega)|^2}{[\Gamma_2(t_m) + \gamma_2]/2 - i\Delta + i\omega} \right\}. \quad (33)$$

Equation (33) is the sum of two terms. The first one, κ_0 , gives the ionization probability in the absence of the dressing laser. The second term involves the convolution of a complex Lorentzian profile with the power spectrum of the two-photon Rabi frequency. The shape of this term [i.e. the dependence on the detuning $\Delta \equiv D_{eff}(t_m)$ at maximum

intensity] depends strongly on the relationship between the quantity $\Gamma_2(t_m) + \gamma_2$ and the bandwidth $\Delta\omega \simeq 1/\tau_p$ of the two-photon Rabi frequency $\tilde{\Omega}(\omega)$.

For purposes of illustration we assume a Gaussian shape for the probe and dressing laser pulses

$$\mathcal{E}_i(t) = \mathcal{E}_{i0} \exp\left[-\frac{t^2}{2\tau_i^2}\right]. \quad (34)$$

We furthermore assume that only one continuum is involved in the process (this implies that initial and final states have angular momentum $\ell = 0$). Then Eqn. (33) can be written as

$$\frac{\kappa}{\kappa_0} = 1 - \text{Re} \left[\frac{(iq-1)^2\tau_0^2}{\sqrt{\pi}\tau_p} \int_{-\infty}^{+\infty} d\omega \frac{(\Gamma_d/2) \exp[-(\omega\tau_0)^2]}{(\Gamma_d + \gamma_2)/2 - i\Delta + i\omega} \right], \quad (35)$$

where the time scale τ_0 is defined by

$$1/\tau_0^2 = 1/\tau_p^2 + 1/\tau_d^2.$$

In Eqn. (35) Γ_d is the ionization rate of the state 2 with the dressing field, for $t = t_m = 0$. We shall refer to Eqn. (35) as the finite-bandwidth approximation.

For further simplification we neglect spontaneous emission from state 2 (for very short pulses $\gamma_2\tau_p \ll 1$) and assume the dressing pulse to be long, so one can set $\tau_0 = \tau_p$. We obtain

$$\frac{\kappa}{\kappa_0} = 1 - \text{Re} \left[\frac{(iq-1)^2\tau_p}{\sqrt{\pi}} \int_{-\infty}^{+\infty} d\omega \frac{(\Gamma_d/2) \exp[-(\omega\tau_p)^2]}{\Gamma_d/2 - i\Delta + i\omega} \right], \quad (36)$$

Eqn. (36), taken with Eqn. (28), provides an analytic expression for the shape of LICS in the pulsed fields. It is a superposition of two profiles: convolution of two symmetric profiles, a Lorentzian and a Gaussian (i.e. a Voigt profile), proportional to $(1 - q^2)$; and a convolution of an asymmetric dispersion-like profile with a Gaussian one, proportional to $2q$. Figure 13 shows examples of LICS calculated using Eqn. (36) for different $\Gamma_d\tau_p$. We used $q = 0.73$, appropriate for the helium states relevant to our experiment.

For short pulses ($\tau_p \leq 1/\Gamma_d$) the LICS is broad, with only minor (if any) enhancement and a small dip. For longer pulses the LICS is more pronounced. Full suppression is approached for $\tau_p \geq 10/\Gamma_d$. Figure 14 shows the dependences of $\Delta_{min}\tau$ and $\Delta_{max}\tau$ on the dimensionless parameter $\Gamma_d\tau_p$ for $q = 0.73$. For $\Gamma_d\tau_p \leq 10$ the pulsed nature of the probe laser affects the frequencies at which the dip and enhancement of the LICS profile are observed. For a pulsed probe laser one can not obtain complete suppression of the ionization probability (see Fig. 15). However, for $\Gamma_d\tau_p = 10$ the ionization rate of the center of the dip is only 1% of the rate far from resonance.

C. Corrections to stationary LICS

It is known [39] that for the stationary limit the effective detuning $\Delta = \Delta_{min}$ of the dip and of the enhancement, $\Delta = \Delta_{max}$, are

$$\Delta_{min} = q\frac{\Gamma_d}{2}, \quad \Delta_{max} = -\frac{\Gamma_d}{2q}. \quad (37)$$

The separation w between the dip and the enhancement is proportional to the ionization rate Γ_d , modified by the Fano q parameter:

$$w \equiv \Delta_{min} - \Delta_{max} = \frac{\Gamma_d}{2} \left(q + \frac{1}{q} \right). \quad (38)$$

For pulsed excitation the stationary results in Eqns. (37) must be modified. For $\Gamma_d\tau_p \gg 1$ one can find perturbation-theory solutions for Δ_{min} and Δ_{max} which replace Eqn. (37) with the approximations

$$\Delta_{min} = q\frac{\Gamma_d}{2} \left(1 + \frac{6}{(q^2 + 1)(\Gamma\tau_p)^2} \right), \quad \Delta_{max} = -\frac{\Gamma_d}{2q} \left(1 + \frac{6}{(q^2 + 1)(\Gamma_d\tau_p)^2} \right), \quad (39)$$

showing that the width w of the LICS is dependent on the probe-pulse duration τ_p ,

$$w = \frac{\Gamma_d}{2} \left(q + \frac{1}{q} \right) \left(1 + \frac{6}{(q^2 + 1)(\Gamma_d \tau_p)^2} \right). \quad (40)$$

In this case the values of the parameter κ for the effective detuning $\Delta = \Delta_{min}$ ($\kappa = \kappa_{min}$) and for $\Delta = \Delta_{max}$ ($\kappa = \kappa_{max}$) are determined by the expressions

$$\frac{\kappa_{min}}{\kappa_0} = \frac{2}{(q^2 + 1)(\Gamma_d \tau_p)^2} \quad (41)$$

$$\frac{\kappa_{max}}{\kappa_0} = (q^2 + 1) \left(1 - \frac{2q^4}{(q^2 + 1)^2 (\Gamma_d \tau_p)^2} \right). \quad (42)$$

Equations (37) - (42) show how the transient nature of pulsed LICS affects the profile, raising the minimum value of the ionization probability in the dip, lowering the enhancement, and increasing the width of the profile.

D. The quasistationary case

The previous analysis shows that the influence of the probe laser pulse duration τ_p (or the transit time of atoms across a probe beam) on the shape of the LICS is important if the dressing-pulse intensity is not very large, $\Gamma_d \tau_p \leq 10$. For larger Γ_d one can neglect the delay in the formation of coherence during the pulses. This means that we can assume $\frac{d}{dt} [h_2^{(1)}(t)] = 0$ in Eqn. (25) and can write, for any τ_p ,

$$h_2^{(1)}(t) = \frac{(iq - 1)\Omega(t)}{\Gamma_2(t) + \gamma_2 - i2D_{eff}(t)}. \quad (43)$$

Then Eqn. (29) for the parameter κ becomes

$$\kappa = \kappa_0 - \text{Re} \left[(iq - 1)^2 \int_{-\infty}^{\infty} dt' \frac{\Omega(t')^2}{\Gamma_2(t') + \gamma_2 - i2D_{eff}(t')} \right]. \quad (44)$$

This equation involves a weighted time integration, rather than the frequency integration of Eqn. (33). It presents the LICS profile as a time-averaged Fano-Cooper or Breit-Wigner profile. The observed profile is affected by the time dependence of the width $\Gamma_2(t)$ and the effective detuning $D_{eff}(t)$ during the interaction.

E. Stationary case, multiple continua

Note that even in the case of a time-independent dressing-laser field the LICS profile parameterized as in Eqn. (2) must include the term σ_b when coupling occurs to more than one photoionization continuum. To illustrate this point, we assume for simplicity that the probe pulse is much shorter than the dressing pulse, $\tau_p \ll \tau_d$. We also neglect spontaneous emission from state 2, so that $\gamma_2 = 0$. Then Eqn. (44) can be written in the form of Eqn. (3) with

$$\Gamma_d = \alpha \sum_j \Gamma_{2d}^{(j)}(t_m), \quad \Gamma_0 = (1 - \alpha) \sum_j \Gamma_{2d}^{(j)}(t_m). \quad (45)$$

The parameter α , describing the effect of multiple continua, is

$$\alpha = \frac{\int_{-\infty}^{\infty} dt \left(\sum_j \sqrt{\Gamma_{1p}^{(j)}(t) \Gamma_{2d}^{(j)}(t)} \right)^2}{\int_{-\infty}^{\infty} dt \left(\sum_j \Gamma_{1p}^{(j)}(t) \right) \left(\sum_j \Gamma_{2d}^{(j)}(t) \right)} \leq 1. \quad (46)$$

The shape of the LICS depends strongly on the relationship between the ionization rates $\Gamma_{lk}^j(t)$. If $\alpha \neq 1$ the enhancement of the ionization is smaller and the ionization dip does not reach zero as it does for only one continuum, see

Eqn. (44). The minimum and maximum values of κ provide information needed to determine the parameters α and q , using the formulas

$$\begin{aligned}\kappa_{min}/\kappa_0 &= 1 - \alpha, \\ \kappa_{max}/\kappa_0 &= 1 + \alpha q^2.\end{aligned}\tag{47}$$

The parameter α will be unity if there is a single continuum, as occurs for helium when the bound states have orbital angular momentum $\ell = 0$. (In this case the angular momentum of the continuum states is $\ell = 1$.) Alternatively, one has $\alpha \simeq 1$ for a transition within the triplet manifold, ${}^3S_1 - {}^3S_1$. In this case three continua are involved in the process: 3P_0 , 3P_1 , and 3P_2 . With the neglect of spin interactions, the radial matrix elements for the bound-continuum transitions do not depend on the angular momentum j ; with this approximation one finds $\alpha = 1$ from Eqn. (46). In all other cases $\alpha < 1$.

F. Quasistationary case, single continuum

Let us consider the case $\alpha = 1$, so that $\Omega^2(t) = \Gamma_1(t)\Gamma_2(t)$ (only one continuum is involved in the process). Then Eqn. (44) for the parameter κ can be written as

$$\kappa = \int_{-\infty}^{\infty} dt \Gamma_1(t) \frac{[x(t) + q]^2}{x(t)^2 + 1}, \tag{48}$$

where the variable $x(t)$ is the ratio of a time varying Stark-shifted detuning and a time varying width $\Gamma_2(t)$.

$$x(t) = -\frac{2D_{eff}(t)}{\Gamma_2(t)}.\tag{49}$$

Eqn. (48) gives the LICS profile as the integral of a time-dependent single-continuum profile $f(x) = (x + q)^2/(x^2 + 1)$ weighted by the variable $\Gamma_1(t)$. Consequently the resulting lineshape, Eqn. (48) is different from the function $f(x)$: the dip does not drop to zero, and the enhancement is smaller. The value of κ in the dip is determined by the Stark shift and power broadening. It can be estimated for Gaussian pulses and $\tau_p \ll \tau_d$ to be

$$\frac{\kappa_{min}}{\kappa_0} = \frac{1}{2} \frac{\{q + 2[S_2(0) - S_1(0)]/\Gamma_2(0)\}^2 \tau_p^4}{q^2 + 1 \tau_d^4}.\tag{50}$$

This formula shows the minimum value of the photoionization suppression that can be reached for the quasistatic case.

G. Comparison between theories

Our primary comparison between experiment and theory was made by means of numerical simulation – solving the coupled ordinary differential equations, Eqn. (12). It is instructive to compare the results of those computations with several analytic approximations discussed in the previous paragraphs. Figure 16 presents such a comparison. The full-line curve shows the results obtained by integrating Eqn. (12). The dashed line is the finite-bandwidth approximation of Eqn. (35). The dotted line is the quasistationary approximation of Eqn. (44). As can be seen, all three curves are very close to each other. For these plots the value of $\Gamma_d \tau_p$ is 6.4. If this quantity were larger the results would approach the dotted line (the quasistationary limit) even closer.

V. CONCLUSIONS

We have presented a detailed set of observations of LICS profiles obtained when coupling two states of metastable helium to the same continuum by means of pulsed lasers. The profiles exhibit both enhanced and suppressed photoionization, at appropriate wavelengths, for a narrow LICS in an otherwise flat continuum. Photoionization suppression, very pronounced for these observations, shows the presence of population trapping.

We have described a simple single-electron model potential whose wavefunctions provide remarkably good values for atomic parameters. We have shown, in an appendix, that examples of oscillator strengths computed with this potential are very close to values obtained using more elaborate methods of computing wavefunctions.

We have shown that solutions of the appropriate coupled differential equations, using atomic parameters (Stark shifts and Rabi frequencies) computed with the model potential, provide excellent fits to our experimental data.

We have developed analytic approximations to the photoionization probability produced by pulsed laser pairs, and we have shown that these can provide a good approximation to the more elaborate and time-consuming solution of differential equations.

ACKNOWLEDGMENTS

The authors thank R. Unanyan, M. Shapiro and P.L. Knight for valuable discussions, and E. Paspalakis for a preprint. LY is grateful to the Deutsche Forschungsgemeinschaft for support of his visit to Kaiserslautern. BWS and KB acknowledge support from a NATO travel grant. BWS thanks the Alexander von Humboldt Stiftung for a Research Award; his work is supported in part under the auspices of the U.S. Department of Energy at Lawrence Livermore National Laboratory under contract W-7405-Eng-48. This work received partial support by the EU network "Laser Controlled Dynamics of Molecular Processes and Applications", ERB-CH3-XCT-94-0603, the German-Israel Foundation. and the Deutsche Forschungsgemeinschaft.

APPENDIX A: ESTIMATING FANO PARAMETERS

To extract parameters from resonance profiles of either experimental data or simulations we carried out least-squares fits. Less elaborate estimates of the parameters can be obtained by inspection of the profiles.

Consider the profile function proposed by Fano and Cooper to describe an autoionization resonance, with resonance frequency ω_R and width Γ , in the presence of nonresonant background. The photoionization cross section is expressible in the Fano form

$$\sigma(\omega) = \sigma_b(\omega) + \sigma_a \frac{(x + q)^2}{x^2 + 1}, \quad (\text{A1})$$

where q is the dimensionless Fano q parameter and x is a dimensionless detuning,

$$x \equiv (\omega - \omega_R)/(\Gamma/2). \quad (\text{A2})$$

Neglect of the slow variation of σ_b with frequency leads to a profile which has a maximum, σ_{max} , at $\omega = \omega_{max}$, when $x = x_{max} \equiv 1/q$. It has a minimum, σ_{min} , at $\omega = \omega_{min}$, when $x = x_{min} \equiv -q$. It follows that a measurement of the extrema values of the cross section, σ_{max} and σ_{min} , and the associated frequencies ω_{max} and ω_{min} , together with the asymptotic cross section $\sigma(\infty)$ obtained far from resonance, can be used to determine the various parameters of the profile:

$$\sigma_b = \sigma_{min}, \quad (\text{A3})$$

$$\sigma_a = \sigma(\infty) - \sigma_{min}, \quad (\text{A4})$$

$$q = \frac{\sigma_{max} - \sigma(\infty)}{\sigma(\infty) - \sigma_{min}}. \quad (\text{A5})$$

Note that if the resonance formula is applied to a case for which $\sigma_b = 0$ (i.e. there are no additional contributions to background apart from the continuum in which the resonance is embedded), and if the LICS profile is normalized such that $\sigma_a = 1$, then $\sigma_{min} = 0$ and $\sigma(\infty) = 1$, so the expression for q becomes

$$q = \sqrt{\sigma_{max} - 1}. \quad (\text{A6})$$

Once q is known, the width parameter Γ can be determined from the measured frequencies of the extrema, using the expression

$$\Gamma = (\omega_{max} - \omega_{min}) \frac{q}{2(1 + q^2)} = \pi(\nu_{max} - \nu_{min}) \frac{q}{(1 + q^2)}. \quad (\text{A7})$$

The resonance frequency ω_R is obtainable from the expression

$$\omega_R = \frac{1}{2}(\omega_{max} + \omega_{min}) - \Gamma \frac{(1 - q^2)}{4q}. \quad (\text{A8})$$

APPENDIX B: THE MODEL POTENTIAL METHOD

1. The Radial Equation

When we introduce a separation of variables

$$\psi(\mathbf{r}) = R(r)Y(\theta, \phi) = r^{-1}P(r)Y(\theta, \phi), \quad (\text{B1})$$

into the Schrödinger equation for a particle of energy E , mass m and charge $-e$ moving in a central potential $V(r)$ we obtain the differential equation

$$\left[\frac{\hbar^2}{2m} \left(\frac{\partial^2}{\partial r^2} - \frac{\mathbf{L}^2}{r^2} \right) - V(r) + E \right] P(r)Y(\theta, \phi) = 0. \quad (\text{B2})$$

For an attractive Coulomb potential of charge Ze the central potential is

$$V(r) = \left(\frac{e^2}{4\pi\epsilon_0} \right) \frac{Z}{r}.$$

We take $Y(\theta, \phi)$ to be an eigenfunction of \mathbf{L}^2 , either a single spherical harmonic $Y_{\ell m}(\theta, \phi)$ or any combination of spherical harmonics with common value of ℓ , so that the differential operator \mathbf{L}^2 can be replaced by the eigenvalue $\ell(\ell + 1)$. It is useful, and customary, to introduce the Bohr radius a_0 as the unit of length and to express energies in multiples of the atomic unit of energy E_{AU}

$$a_0 = \frac{4\pi\epsilon_0\hbar^2}{me^2}, \quad E_{AU} = \frac{e^2}{4\pi\epsilon_0 a_0} = \frac{\hbar^2}{m(a_0)^2}. \quad (\text{B3})$$

The result is the radial equation

$$\left[\frac{d^2}{dr^2} - \frac{\ell(\ell + 1)}{r^2} - 2V(r) + 2E \right] P(r) = 0. \quad (\text{B4})$$

This equation has bounded solutions for any positive energy, $E > 0$, while for negative energies it has bounded solutions for a set of discrete values, the bound states of the potential $V(r)$ with angular momentum ℓ .

2. Effective potentials

A popular approach to the determination of radial functions is the quantum-defect method originally developed by Bates and Damgaard [50]. It was used for calculating the ionization rates for helium in [51–53]. This method uses solutions to the radial equation for a Coulomb potential, but forces the bound energies to take specified values. Unfortunately this requirement yields functions which diverge at small r , and this poses difficulties in the computation of Stark shifts and two-photon Rabi frequencies when the laser frequency is large enough to cause ionization.

As was shown in [54] the use of a model potential for the calculation of the atomic parameters such as dynamical polarizabilities, Stark shifts, multiphoton ionization rates is convenient. This method is based on the pseudopotential theory [55–57]. Because an exact analytical expression for the pseudopotential cannot be derived a number of model potential was considered.

3. Coulomb potentials

When the effective potential is a Coulomb potential for a charge Ze radial equation is the *hydrogenic radial equation*

$$\left[\frac{d^2}{dr^2} - \frac{\ell(\ell + 1)}{r^2} + \frac{2Z}{r} + 2E \right] P(r) = 0. \quad (\text{B5})$$

As written here, the equation for a Coulomb potential involves three parameters: the nuclear charge Z , the angular momentum ℓ , and the energy E . Rather than use the energy E , it proves useful to introduce alternative parameters. When E is negative useful real-valued parameters are K and ν ,

$$E = -\frac{(\hbar K)^2}{2m} = -\left(\frac{me^2}{4\pi\epsilon_0\hbar} \right)^2 \frac{Z^2}{2\nu^2} \quad \text{or} \quad K = \frac{Z}{a_0\nu}. \quad (\text{B6})$$

The quantity $\hbar K$ is the *rms* momentum, while $1/\nu$ is proportional to the mean value of Z/r . When E is positive the useful real-valued parameters are k and η ,

$$E = \frac{(\hbar k)^2}{2m} = \left(\frac{me^2}{4\pi\epsilon_0\hbar} \right)^2 \frac{Z^2}{2\eta^2} \quad \text{or} \quad k = \frac{Z}{a_0\eta}. \quad (\text{B7})$$

The *rms* momentum is now $\hbar k$.

For a purely Coulomb potential, with nuclear charge Z , the allowed bound state energies are given by the Bohr formula,

$$E_n = -\frac{Z^2}{2n^2} \quad (\text{B8})$$

and are parameterized by the integer principal quantum number n . When the potential deviates from a purely Coulomb potential, then the energies no longer fit this pattern. Often, however, they fit the simple pattern

$$E_{n\ell} = -\frac{Z^2}{2(n - \delta_\ell)^2}, \quad (\text{B9})$$

where δ_ℓ is the quantum defect. There are several ways of constructing wavefunctions associated with such energies.

4. The Radial Functions

Consider a generalization of the negative-energy hydrogenic radial equation

$$\left[\frac{d^2}{dr^2} - \frac{\lambda(\lambda + 1)}{r^2} + \frac{2Z}{r} - \left(\frac{Z}{\nu} \right)^2 \right] P(r) = 0 \quad (\text{B10})$$

with the energy (in atomic units) defined as

$$E = -\frac{Z^2}{2\nu^2}. \quad (\text{B11})$$

This radial equation has negative-energy solutions of the form

$$P(r) = \mathcal{N} \exp\left(-\frac{Zr}{\nu}\right) r^{\lambda+1} {}_1F_1(-\nu + \lambda + 1; 2\lambda + 2; \frac{2Zr}{\nu}), \quad (\text{B12})$$

where ${}_1F_1(a; c; x)$ is a confluent hypergeometric function (Kummer function),

$$\begin{aligned} {}_1F_1(a; c; x) &= 1 + \frac{a}{c} \frac{x}{1!} + \frac{a(a+1)}{c(c+1)} \frac{x^2}{2!} + \dots \\ &= \sum_{n=0}^{\infty} \frac{\Gamma(a+n)}{\Gamma(a)} \frac{\Gamma(c)}{\Gamma(c+n)} \frac{x^n}{\Gamma(n+1)} \end{aligned} \quad (\text{B13})$$

and where \mathcal{N} is a normalization constant, expressible variously as

$$\begin{aligned} \mathcal{N} &= \left(\frac{2Z}{\nu} \right)^\ell \frac{2\sqrt{Z}}{\Gamma(2\ell + 2)} \sqrt{\frac{dE}{d\nu}} \sqrt{\frac{\Gamma(\nu + \lambda + 1)}{\Gamma(\nu - \lambda)}} \\ &= \left(\frac{2Z}{\nu} \right)^\ell \frac{2Z^{3/2}}{\nu^2} \frac{1}{\Gamma(2\ell + 2)} \sqrt{\frac{\Gamma(n_r + 2\lambda + 2)}{\nu\Gamma(n_r + 1)}} \end{aligned} \quad (\text{B14})$$

where $n_r = \nu - \lambda - 1$ is the radial quantum number. The radial functions can also be written in terms of Laguerre polynomials

$$\begin{aligned} P(r) &= \left(\frac{2Z}{\nu} \right)^\ell \frac{2Z^{3/2}}{\nu^2} \sqrt{\frac{\Gamma(n_r + 1)}{\Gamma(n_r + 2\lambda + 2)}} \\ &\quad \times \exp\left(-\frac{Zr}{\nu}\right) r^{\lambda+1} L_{n_r}^{(2\lambda+1)}\left(\frac{2Zr}{\nu}\right) \end{aligned} \quad (\text{B15})$$

The energy-normalized radial wavefunctions for positive energy $E = k^2/2$ can be written as [60]

$$\begin{aligned} P_{E\ell}(r) &= \frac{|\Gamma(\lambda + 1 + i\eta)|}{\Gamma(2\lambda + 2)} \frac{\exp(\pi\eta/2)}{\sqrt{2\pi k}} (2kr)^{\lambda+1} \\ &\quad \times \exp(-ikr) r^{\lambda+1} {}_1F_1(\lambda + 1 + i\eta; 2\lambda + 2; 2ikr), \end{aligned} \quad (\text{B16})$$

where $k = \sqrt{2E}$ is the mean momentum and $\eta = Z/k$ is the Coulomb parameter.

5. Examples

c. Hydrogenic Ions When λ is an integer, $\lambda = \ell$, as is the case for hydrogen, then ν must be an integer, the principal quantum number n , in order that the hypergeometric function remain bounded:

$$\text{if } \lambda = \ell \text{ then } \nu = n. \quad (\text{B17})$$

This condition fixes the energy E by the Bohr formula

$$E_n = -\frac{Z^2}{2n^2}. \quad (\text{B18})$$

d. Screened Hydrogenic Functions One method to obtain a wavefunction for one or two low-lying bound states is to introduce an effective nuclear charge Z^* through the definition

$$Z_{n\ell}^* = \sqrt{-2E_{n\ell}}. \quad (\text{B19})$$

This approach maintains the quantum numbers n and ℓ , and deals with well behaved bound functions.

e. The Quantum Defect Method One approach to obtaining radial functions with the desired energies is to simply let ν be defined to produce the desired energies,

$$\nu = \nu_n = n - \delta_\ell, \quad (\text{B20})$$

while retaining the integer values for ℓ . However, this approach, commonly termed the *quantum defect method*, does not produce radial functions which remain bounded for all distances. In order that the hypergeometric function be a polynomial, it is necessary that the first argument be an integer, the radial quantum number n_r ,

$$n_r = \lambda + 1 - \nu. \quad (\text{B21})$$

f. The Effective Potential However, we can choose λ to be a parameter fixed by ℓ and a given energy: we write the (integer) radial quantum number as

$$n_r = -n + \ell + 1 = -\nu + \lambda + 1. \quad (\text{B22})$$

This means that the energy is given by the quantum defect formula

$$E_{n\ell} = -\frac{Z^2}{2(n + \lambda - \ell)^2} \quad (\text{B23})$$

and, in turn, that the parameter ν is

$$\nu_{n\ell} \equiv \sqrt{-\frac{Z^2}{2E_{n\ell}}} = n + \lambda - \ell. \quad (\text{B24})$$

One can use the lowest energy value E_1 (i.e. the ionization energy) to define the quantum defect, so that one has, for specified ℓ , the effective orbital angular momentum

$$\lambda = \ell - 1 + \sqrt{-\frac{Z^2}{2E_1}}. \quad (\text{B25})$$

Then the n th radial function for specified ℓ is

$$P(r) = \mathcal{N} r^{\lambda+1} \exp\left(-\frac{Zr}{\nu_{n\ell}}\right) {}_1F_1\left(-n + \ell + 1; 2\lambda + 2; \frac{2Zr}{\nu_{n\ell}}\right). \quad (\text{B26})$$

6. Dipole Transition Moments

The radial matrix elements of the dipole transition moment for transition between states with the radial quantum numbers n_a and n_b and with effective angular momentum ℓ_a and ℓ_b respectively is

$$R_{a,b} \equiv \int_0^\infty P_a(r)P_b(r)r dr. \quad (\text{B27})$$

Many authors have presented expressions for these matrix elements when the radial functions are those of hydrogen-like atoms [61–72]. We have found that a convenient expression is

$$\begin{aligned} R_{a,b} &= \frac{1}{4Z} \left(\frac{2\nu_b}{\nu_a + \nu_b} \right)^{\lambda_a+2} \left(\frac{2\nu_a}{\nu_a + \nu_b} \right)^{\lambda_b+2} \frac{\Gamma(\lambda_a + \lambda_b + 4)}{\Gamma(2\lambda_a + 2)\Gamma(2\lambda_b + 2)} \\ &\times \left[\frac{\Gamma(\nu_a + \lambda_a + 1)\Gamma(\nu_b + \lambda_b + 1)}{\Gamma(n_a + 1)\Gamma(n_b + 1)} \right]^{1/2} \\ &\times F_2 \left(\lambda_a + \lambda_b + 4; -n_a, -n_b; 2\lambda_a + 2, 2\lambda_b + 2; \frac{2\nu_b}{\nu_a + \nu_b}, \frac{2\nu_a}{\nu_a + \nu_b} \right) \end{aligned} \quad (\text{B28})$$

where F_2 is the generalized hypergeometric function of two arguments [73]:

$$\begin{aligned} F_2(\alpha; \beta_1, \beta_2; \gamma_1, \gamma_2; x, y) &= \\ &= \sum_{n,m=0}^{\infty} \frac{\Gamma(\alpha + n + m)}{\Gamma(\alpha)} \frac{\Gamma(\beta_1 + n)}{\Gamma(\beta_1)} \frac{\Gamma(\beta_2 + m)}{\Gamma(\beta_2)} \\ &\times \frac{\Gamma(\gamma_1)}{\Gamma(\gamma_1 + n)} \frac{\Gamma(\gamma_2)}{\Gamma(\gamma_2 + m)} \frac{x^n}{\Gamma(n + 1)} \frac{y^m}{\Gamma(m + 1)}. \end{aligned} \quad (\text{B29})$$

When $\beta_1 = -n_a$ and $\beta_2 = -n_b$ are negative integers the series terminates and F_2 is then a polynomial in x and y .

For transitions from a bound state a to the continuum state b one can write

$$\begin{aligned} R_{a,b} &\equiv \int_0^\infty P_a(r)P_b(r)r dr \\ &= \frac{|\Gamma(\lambda_b + 1 + iZ/k_b)|\Gamma(\lambda_a + \lambda_b + 4)}{(2k)^3\Gamma(2\lambda_a + 2)\Gamma(2\lambda_b + 2)} \left[\frac{k_b\Gamma(\nu_a + \lambda_a + 1)}{2\pi Z\Gamma(n_a + 1)} \right]^{1/2} \\ &\times \left(\frac{2k\nu_a}{Z + ik_b\nu_a} \right)^{\lambda_b+3} \left(\frac{2Z}{Z + ik_b\nu_a} \right)^{\lambda_a+1} \frac{2}{\nu_a} \exp\left(\frac{\pi Z}{2k_b}\right) \\ &\times F_2 \left(\lambda_a + \lambda_b + 4; -n_a, \lambda_b + 1 + i\frac{Z}{k_b}; 2\lambda_a + 2, 2\lambda_b + 2; \frac{2Z}{Z + ik_b\nu_a}, \frac{2ik_b\nu_a}{Z + ik_b\nu_a} \right). \end{aligned} \quad (\text{B30})$$

In this case the function F_2 is the sum of finite number of terms that are proportional to the hypergeometric function of one argument

$$y = \frac{2ik_b\nu_a}{Z + ik_b\nu_a}. \quad (\text{B31})$$

Using the expression (B29) and (B30) one can compute, with sufficiently high accuracy, values of the ionization rates, Stark shifts and two-photon Rabi frequencies.

7. Needed parameters

For Raman transitions between S states (involving only one P continuum) the ionization rates of Eqn. (15), Stark shifts of Eqn. (16) and two-photon Rabi frequency of Eqn. (18) can be expressed in simpler form [12]:

$$\Gamma_{nj} = (4\pi^2/3) \alpha I_j |f(n, \omega_j + E_n)|^2, \quad (\text{B32})$$

$$\begin{aligned} S_{nj} = & (4\pi/3) \alpha I_j \sum_m |g(n, m)|^2 \left(\frac{1}{-E_m + E_n + \omega_i} + \frac{1}{-E_m + E_n - \omega_i} \right) \\ & + (4\pi/3) \alpha I_j \int dE |f(n, E)|^2 \left(\frac{1}{-E + E_n + \omega_i} + \frac{1}{-E + E_n - \omega_i} \right), \end{aligned} \quad (\text{B33})$$

where α is the Sommerfeld fine-structure constant. The Fano q parameter is

$$\begin{aligned} q = & \frac{1}{\pi} \left[\sum_m g(1, m)g(2, m) \left(\frac{1}{E_m - E_1 - \omega_p} + \frac{1}{E_m - E_1 + \omega_d} \right) + \right. \\ & \left. + \int dE f(1, E)f(2, E) \left(\frac{1}{E - E_1 - \omega_p} + \frac{1}{E - E_1 - \omega_d} \right) \right] / [f(1, \omega_1 + E_1)f(2, \omega_2 + E_2)]. \end{aligned} \quad (\text{B34})$$

Here $g(n, m) \equiv R_{n0, m1}$, $f(n, E) \equiv R_{n0, E1}$ are the radial matrix elements determined by the expressions (B28) and (B30).

One can see that for the calculation of the Stark shifts and the Fano q parameter we must find the infinite sums in (B33) and (B34). In the present calculations we usually restrict the sum to the first 200 terms. This gives an accuracy of the infinite sum that is in any case much greater than the accuracy of the model potential method. The integral over the continuum spectrum after the transformation is [54]

$$\int_0^\infty \frac{f(x)}{x-a} dx = \int_0^{2a} \frac{f(x) - f(a)}{x-a} dx + \int_{2a}^\infty \frac{f(x)}{x-a} dx \quad (\text{B35})$$

was computed by Gauss quadrature.

APPENDIX C: NUMERICAL VALIDATION OF MODEL POTENTIAL

1. The Wavefunctions

Theoretical prediction of a LICS structure requires computation of the ionization rates Eqn. (15), Stark shifts Eqn. (16) and two-photon Rabi frequency Eqn. (18) using realistic wavefunctions. Because these various parameters all require summations over many discrete states and integration over many continuum states, it is desirable to have wavefunctions which require as little computational effort as possible, while still providing accurate depiction of the essential properties of the active electron. We have found that a simple single-electron model potential satisfies both these requirements. Appendix B describes the mathematics of this method for computing matrix elements. As noted there, a single empirically determined parameter λ_ℓ fixes the potential, and hence all the wavefunctions, for each orbital angular momentum ℓ .

2. Calculations of the parameters of He

Because the singlet and triplet systems of He interact only weakly, we consider each system to be independent. For each system we calculate λ_ℓ using the experimental term values from the NBS tables [74]. Some results of these calculations are shown in table IV and in table V. As one can see from these tables, the value of λ_l depends weakly on the energy. The radial transition moments are also slowly varying functions of energy. However, the Stark shifts and two-photon Rabi frequency are very sensitive to the energy of intermediate states: when an accidental resonance occurs then the use of an approximate energy value determined by ν_n can lead to large inaccuracy.

TABLE IV. The values of the energies, parameters λ_ℓ and ν_n for singlet He

	$E, \text{ cm}^{-1}$	λ_ℓ	$\nu_n l$		$E, \text{ cm}^{-1}$	λ_ℓ	$\nu_n l$		$E, \text{ cm}^{-1}$	λ_l	$\nu_n l$
$2^1 S$	-32032.3	-.149	1.851	$2^1 P$	-27175.8	1.010	2.010				
$3^1 S$	-13445.9	-.143	2.857	$3^1 P$	-12101.5	1.011	3.011	$3^1 D$	-12205.7	1.998	2.998
$4^1 S$	-7370.5	-.141	3.859	$4^1 P$	-6818.1	1.012	4.012	$4^1 D$	-6864.2	1.998	3.998
$5^1 S$	-4647.2	-.141	4.859	$5^1 P$	-4368.3	1.012	5.012	$5^1 D$	-4392.4	1.998	4.998
$6^1 S$	-3195.8	-.140	5.860	$6^1 P$	-3035.8	1.012	6.012	$6^1 D$	-3049.9	1.998	5.998
$7^1 S$	-2331.8	-.140	6.860	$7^1 P$	-2231.6	1.013	7.013	$7^1 D$	-2240.6	1.998	6.998
$8^1 S$	-1777.0	-.139	7.861	$8^1 P$	-1709.4	1.012	8.012	$8^1 D$	-1715.2	1.998	8.998
$9^1 S$	-1397.9	-.140	8.860	$9^1 P$	-1351.1	1.012	9.012	$9^1 D$	-1355.5	1.998	9.998
$10^1 S$	-1128.6	-.140	9.860	$10^1 P$	-1094.8	1.013	10.013	$10^1 D$	-1097.9	1.998	9.998
				$15^1 P$	-486.9	1.013	15.013				
				$20^1 P$	-274.0	1.013	20.013				
cont.		-.139		cont.		1.013		cont.		1.998	

TABLE V. The values of the energies, parameteres λ_ℓ and ν_n for triplet He

	$E, \text{ cm}^{-1}$	λ_ℓ	ν_{nl}		$E, \text{ cm}^{-1}$	λ_ℓ	$\nu_{n\ell}$		$E, \text{ cm}^{-1}$	λ_ℓ	$\nu_{n\ell}$
2^3S	-38454.7	-.311	1.689	2^3P	-29223.8	.938	1.938				
3^3S	-15073.9	-.302	2.698	3^3P	-12746.1	.934	2.934	3^3D	-12209.1	1.998	2.998
4^3S	-8012.5	-.299	3.701	4^3P	-7093.5	.933	3.933	4^3D	-6866.2	1.998	3.998
5^3S	-4963.6	-.298	4.702	5^3P	-4509.9	.933	4.933	5^3D	-4393.5	1.998	4.998
6^3S	-3374.5	-.297	5.703	6^3P	-3117.8	.933	5.933	6^3D	-3050.6	1.998	5.998
7^3S	-2442.4	-.297	6.703	7^3P	-2283.3	.933	6.933	7^3D	-2241.0	1.998	6.998
8^3S	-1849.2	-.297	7.703	8^3P	-1743.9	.933	7.933	8^3D	-1715.6	1.998	8.998
9^3S	-1448.6	-.296	8.704	9^3P	-1375.3	.933	8.933	9^3D	-1355.4	1.998	9.998
10^3S	-1165.2	-.296	9.704	10^3P	-1112.4	.932	9.932	10^3D	-1097.7	1.999	9.999
15^3S	-508.4	-.308	14.692	15^3P	-491.9	.936	14.936				
				20^3P	-275.9	.942	19.942				
cont.		-.300		cont.		0.940		cont.		1.998	

3. Accuracy

To demonstrate the accuracy of the model-potential method we display in tables VI and VII the computed oscillator strength for S-P transitions in singlet and triplet He. There is exceptionally good agreement between our values and those obtained with more sophisticated methods. Except for transitions from the ground state, the differences between our values and the more accurate ones are always less than 10%. The lack of accuracy for transitions involving the ground state is expected because here the influence of polarization and exchange effects are greatest.

To test the accuracy of the continuum wavefunctions we have calculated the cross sections for photoionizations from some excited levels. Comparisons of the cross sections calculated with the help of model potential with results of other author are illustrated in Fig. 17, for the $2s \ ^1S_0$ level. One can see that our values, obtained with a very simple approach, are in very good agreement with previous ones obtained by more sophisticated methods. The accuracy of our one-photon bound-bound and bound-free transitions validates the use of model-potential wavefunctions for the calculation of Stark shifts and two-photon Rabi frequency for helium.

TABLE VI. Oscillator strength for transitions between 1^1S and 1^1P -states of He

		2^1P	3^1P	4^1P	5^1P
1^1S	a	0.362	0.082	0.031	0.015
	b	0.276	0.073	0.030	0.015
	c	0.276	0.073	0.030	0.015
2^1S	a	0.375	0.165	0.053	0.024
	b	0.376	0.151	0.049	0.022
	c	0.376	0.151	0.049	0.020
4^1S	a	0.024	0.291	0.859	0.157
	b	0.026	0.308	0.858	0.146
	c	0.026	0.306	0.855	0.150
5^1S	a	0.009	0.053	0.460	1.09
	b	0.010	0.056	0.476	1.08
	c	0.010	0.055	0.470	1.10

^aThe model potential method. ^bThe results of Chen [48]. ^c The results of Schiff *et al* [45].

TABLE VII. Oscillator strength for transitions between 3^3S and 3^3P -states of He

		2^3P	3^3P	4^3P	5^3P
1^3S	a	0.563	0.060	0.024	0.012
	b	0.539	0.064	0.026	0.012
	c	0.539	0.064	0.026	0.013
2^3S	a	0.210	0.908	0.051	0.023
	b	0.209	0.891	0.050	0.023
	c	0.209	0.891	0.050	0.023
4^3S	a	0.033	0.438	1.225	0.044
	b	0.032	0.436	1.215	0.044
	c	0.032	0.436	1.215	0.044
5^3S	a	0.012	0.068	0.669	1.540
	b	0.011	0.068	0.668	1.531
	c	0.011	0.068	0.670	1.530

^aThe model potential method. ^b The results of Chen [48]. ^c The results of Schiff *et al* [45].

-
- [1] A. Messiah, *Quantum Mechanics* (North Holland, New York, 1961)
- [2] K. J. Schafer and K. C. Kulander, Phys. Rev. A **42**, 5794 (1990)
- [3] K. C. Kulander, K. J. Schafer and J. L. Krause, Int. J. Quant. Chem. **25**, 415 (1991)
- [4] J. L. Krause, K. J. Schafer and K. C. Kulander, Phys. Rev. A **45**, 4998 (1992)
- [5] A. Goldberg and B. W. Shore, J. Phys. B. **11**, 3339 (1978)
- [6] E. Frishman and M. Shapiro, Phys. Rev. A **54**, 3310 (1996)
- [7] A. Vardi and M. Shapiro, J. Chem. Phys. **104**, 5490 (1996)
- [8] A. Vardi, D. Abrashkevich, E. Frishman and M. Shapiro, J. Chem. Phys. **107**, 6166 (1997)
- [9] Z. Deng and J. H. Eberly, JOSA B **2**, 486 (1985)
- [10] E. Paspalakis, M. Protopapas and P. L. Knight, Opt. Comm. **142**, 34 (1997)
- [11] E. Paspalakis, M. Protopapas and P. L. Knight, J. Phys. B **31**, 775 (1998)
- [12] L. P. Yatsenko, R. G. Unanyan, K. Bergmann, T. Halfmann and B. W. Shore, Optics Comm. **135**, 406 (1997)
- [13] O. Faucher, D. Charalambidis, C. Fotakis, J. Zhang and P. Lambropoulos, Phys. Rev. Lett. **70**, 3004 (1993)
- [14] O. Faucher, Y. L. Shao and D. Charalambidis, J. Phys. B **26**, L309 (1993)
- [15] U. Fano, Phys. Rev. **124**, 1866 (1961)
- [16] U. Fano and J. W. Cooper, Phys. Rev. **137**, A1364 (1965)
- [17] B. W. Shore, Rev. Mod. Phys. **39**, 429 (1967)
- [18] M. H. R. Hutchinson and K. M. M. Ness, Phys. Rev. Letts. **60**, 105 (1988)
- [19] X. Tang, A. L'Huillier, P. Lambropoulos, M. H. R. Hutchinson and K. M. M. Ness, Phys. Rev. Letts. **62**, 111 (1989)
- [20] Y. L. Shao, D. Charalambidis, C. Fotakis, J. Zhang and P. Lambropoulos, Phys. Rev. Lett. **67**, 3669 (1991)
- [21] S. Cavalieri, F. S. Pavone and M. Matera, Phys. Rev. Lett. **67**, 3673 (1991)
- [22] S. Cavalieri, R. Eramo and L. Fini, J. Phys. B **28**, 1793 (1995)
- [23] S. Cavalieri, R. Eramo, R. Buffa and M. Matera, Phys. Rev. A **51**, 2974 (1995)
- [24] R. Eramo, S. Cavalieri, L. Fini, M. Matera and L. F. DiMauro, J. Phys. B **30**, 3789 (1997)
- [25] T. Halfmann, L. P. Yatsenko, M. Shapiro, B. W. Shore and K. Bergmann, Phys. Rev. A **58**, R46 (1998)
- [26] Z. D. Chen, M. Shapiro and P. Brumer, Phys. Rev. A **52**, 2225 (1995)
- [27] P. Lambropoulos and P. Zoller, Phys. Rev. A **24**, 379 (1981)
- [28] L. I. Pavlov, S. S. Dimov, D. I. Mechikov, G. M. Mileva, K. V. Stamenov and G. B. Altschuler, Phys. Lett **89A**, 441 (1981)
- [29] K. Rzazewski and J. H. Eberly, Phys. Rev. Lett. **47**, 408 (1981)
- [30] K. Rzazewski and J. H. Eberly, Phys. Rev. A **27**, 2026 (1983)
- [31] A. Lami, N. K. Rahman and P. Spizzo, Phys. Rev. A **40**, 2385 (1989)
- [32] A. Lami and N. K. Rahman, Phys. Rev. A **33** 782 (1986)
- [33] K. S. Lam and T. F. George, Phys. Rev. A **35**, 2491 (1986)
- [34] O. Faucher, Y. L. Shao, D. Charalambidis and C. Fotakis, Phys. Rev. a **50**, 641 (1994)
- [35] N. E. Karapanagioti, O. Faucher, Y. L. Shao and D. Charalambidis, Phys. Rev. Letts. **74**, 2431 (1995)
- [36] E. Arimondo, Prog. Optics **35**, 259 (1996)
- [37] B. W. Shore, *The Theory of Coherent Atomic Excitation* (Wiley, N.Y., 1990)
- [38] P. L. Knight, Comm. At. Mol. Phys. **15**, 193 (1984)
- [39] P. L. Knight, M. A. Lauder and B. J. Dalton, Physics Reports **190**, 1 (1990)
- [40] B. W. Shore, Phys. Rev. **171**, 43 (1968)
- [41] M. Crance and M. Aymar, J. Phys. B **13**, L421 (1980)
- [42] B.-N. Dai and P. Lambropoulos, Phys. Rev. A **36**, 5205 (1987)
- [43] T. Nakajima, M. Elk, J. Zhang and P. Lambropoulos, Phys. Rev. A **50**, R913 (1994)
- [44] P. G. Burke and D. D. McVicar, Proc. Phys. Soc.(Lond) **86**, 989. (1965)
- [45] B. Schiff, C. L. Pekeris and 885., Phys. Rev. A **4**, 885 (1971)
- [46] P. W. Langhoff, S. T. Epstein and M. Karplus, Rev. Mod. Phys. **44**, 602 (1977)
- [47] A. Kono and S. Hattori, Phys. Rev. A **29**, 2981 (1984)
- [48] M.-K. Chen, J. Phys. B **27**, 865 (1994)
- [49] N. J. Klystra, E. Paspalaikis and P. L. Knight, J. Phys. B **31**, L719 (1998)
- [50] D. R. Bates and A. Damgaard, Phil. Trans. Roy. Soc. Lond. A **242**, 101 (1949)
- [51] A. Burgess and M. J. Seaton, Mon. Not. R. Astron. Soc. **120**, 121 (1960)
- [52] B. A. Zon, N. L. Manakov and L. P. Rapoport, Sov. Phys. JETP **34**, 515 (1972)
- [53] T. Olsen, P. Lambropoulos, S. E. Wheatley and S. P. Rountree, J. Phys. B **11**, 4167 (1978)
- [54] N. L. Manakov and V. D. Ovsianikov, J. Phys. B **10**, 569 (1977)
- [55] J. C. Philips and L. Kleinman, Phys. Rev. **112**, 685 (1958)
- [56] B. J. Austin, V. Heine and L. J. Sham, Phys. Rev. **127**, 276 (1962)

- [57] J. N. Bardsley, *Case Studies in Atomic Physics* **4**, 299 (1974)
- [58] H. Hellmann, *J. Chem. Phys.* **3**, 61 (1935)
- [59] G. Simons, *J. Chem. Phys.* **55**, 756 (1971)
- [60] L. P. Rapoport, B. A. Zon and N. L. Manakov., *Theory of multiphoton processes in atoms* (Atomizdat, Moscow, 1978)
- [61] L. C. Green, P. P. Rush and D. D. Chandler, *Ap. J. Suppl.* **3**, 37 (1957)
- [62] A. M. Naqvi, *JQSRT* **4**, 597 (1964)
- [63] D. H. Menzel, *Rev. Mod. Phys.* **36**, 613 (1964)
- [64] M. N. Lewis, *Comp. Phys. Comm.* **1**, 325 (1970)
- [65] J. W. Farley and W. H. Wing, *Phys. Rev.* **23**, 2397 (1981)
- [66] K. Omidvar, *At. Data and Nucl. Data Tables* **28**, 1 (1983)
- [67] K. Omidvar, *At. Data and Nucl. Data Tables* **28**, 215 (1983)
- [68] G. W. F. Drake and R. A. Swainson, *Phys. Rev.* **A42**, 1123 (1990)
- [69] D. Hoangbinh, *Astronomy and Astrophysics* **238**, 449 (1990)
- [70] B. Moreno, A. L. Pineiro and R. H. Tipping, *J. Phys. A* **24**, 385 (1991)
- [71] R. Dubey, G. S. Khandelwal and W. M. Pritchard, *J. Phys. B* **24**, 57 (1991)
- [72] K. B. Choudhury, N. C. Deb and S. C. Mukherjee, *Physica Scripta* **54**, 150 (1996)
- [73] A. Erdelyi, ed. *Higher Transcendental Functions* (McGraw-Hill, N.Y., 1953)
- [74] C. E. Moore, *Atomic Energy Levels* (U.S. Government Printing Office, Washington, D.C., 1971)
- [75] M. Aymar and M. Crance, *J.Phys.B: Atom. Molec. Phys.* **13**, 2527 (1980).
- [76] D.W. Norcross, *J.Phys.B: Atom. Molec. Phys.* **4**, 652 (1971).
- [77] V.Jacobs, *Phys. Rev.* **A4**, 939 (1971).

FIG. 1. Laser induced couplings in metastable helium. The probe laser at 294 nm and the dressing laser at 1064 nm couple the metastable singlet state $2s\ ^1S_0$ and the initially unpopulated excited state $4s\ ^1S_0$ through the ionization continuum. For strong laser intensities two-photon ionization (IR and UV) of the metastable triplet state $2s\ ^3S_1$ forms an additional background for the ion signal.

FIG. 2. Layout of experiment, showing atomic beam, discharge, skimmer and lasers. The helium atoms are excited in a pulsed gas discharge. The atomic beam then interacts with the lasers in the center of a capacitor. The ions produced there are accelerated and detected on a microsphere plate.

FIG. 3. REMPI transitions for detecting population in the metastable states of helium. The singlet state $2s\ ^1S_0$ is coupled with pulsed radiation at 397 nm through the excited state $4p\ ^1P_1$ to the ionization continuum. The metastable triplet state $2s\ ^3S_1$ is ionized with laser light at 389 nm through the states $3p\ ^3P_{0,1,2}$.

FIG. 4. Ion signal resulting from the ionization of the metastable states after excitation of the helium atoms in a pulsed gas discharge. The populations are probed by resonant enhanced multiphoton ionization (REMPI) with a pulsed dye laser (bandwidth 6 GHz). The probing transitions are strongly saturation-broadened. In the gas discharge about 90 % of the excited helium atoms are found in the metastable triplet state $2s\ ^3S_1$, and only 10 % are in the singlet state $2s\ ^1S_0$.

FIG. 5. Difference between ion signals with and without IR laser. The probe laser frequency tuned far away from the two-photon resonance where LICS is observed. The pump laser intensity is varied, while the dressing laser intensity is kept constant at $I_S^{(0)} = 226\text{ MW/cm}^2$. The measured data are normalized to the total ionization signal from singlet- and triplet state. Good agreement is found between the experimental values and the calculated results (dashed line).

FIG. 6. LICS for coincident (left side) and delayed (right side) laser pulses, when the dressing laser intensity is varied. The experimental data are compared to results from numerical simulations (dotted lines), including laser intensity fluctuations and integration over the spatial profile of the pump laser. Enhancement as well as strong suppression of ionization are observed.

FIG. 7. Observed and calculated ionization probability of state $2s\ ^1S_0$, as the pump laser intensity is increased. The dressing laser is switched off.

FIG. 8. LICS profile for weak and strong pump laser. The dressing laser intensity is $I_d^{(0)} = 44\text{ MW/cm}^2$ (Fig. 8 a). The probe laser intensity is $I_p^{(0)} = 50\text{ MW/cm}^2$ (Fig. 8 b). Both laser pulses are coincident. With increased pump laser intensity, the maximum enhancement as well as the suppression of ionization is reduced.

FIG. 9. An example of fitting of the experimental data using Eqn. (3). Squares are experimental data, dotted line is the result of fitting, circles are the difference between experimental data and the fit ($\Delta t = 0\text{ ns}$, $I_p^{(0)} = 4\text{ MW/cm}^2$, $I_d^{(0)} = 75\text{ MW/cm}^2$).

FIG. 10. Width parameters vs. intensity of the dressing pulse (see Eqn. (3) and Table I): (1) is the variation of the overall width parameter Γ , (2) is the empirically determined Γ_d , (3) is the calculated photoionization rate Γ_d .

FIG. 11. LICS profile for two approximations: the solid line shows the simulation results for a single pair of pulses, the dotted line shows the profile assuming steady-state conditions ($q = 0.73$, $I_p^{(0)} = 2.5\text{ MW/cm}^2$, $I_d^{(0)} = 38\text{ MW/cm}^2$).

FIG. 12. Dressing pulse and delayed probe pulse ($\Delta t = -5\text{ ns}$, $I_p^{(0)} = 4\text{ MW/cm}^2$, $I_d^{(0)} = 75\text{ MW/cm}^2$).

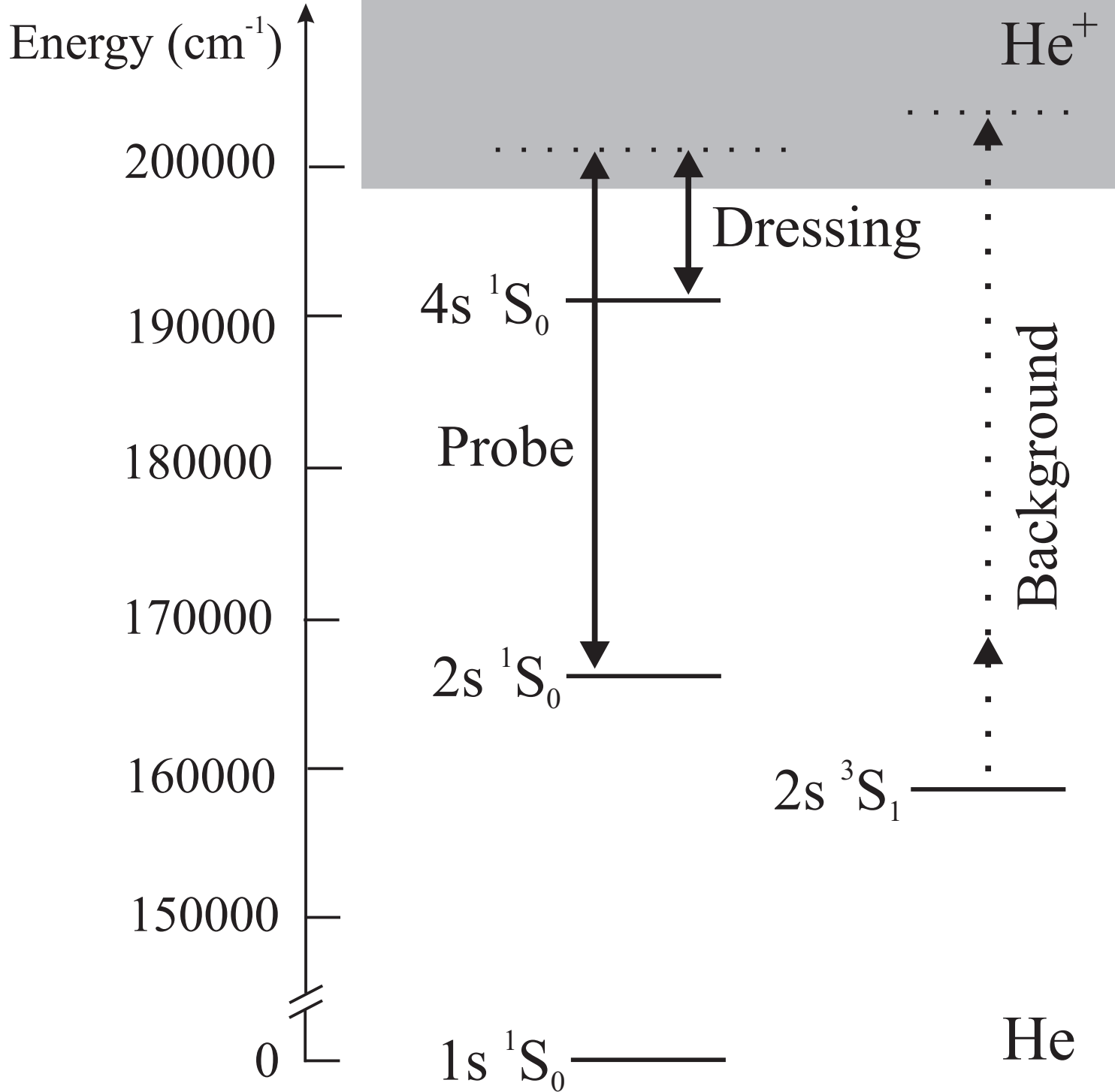
FIG. 13. Plots of κ/κ_0 versus D/Γ_d (detuning in units of the width) for $q = 0.73$ and various values of $\Gamma_d\tau_p$. For given Γ_d this product is proportional to the length of the probe laser pulse.

FIG. 14. Probe laser frequencies at which occurs the minimum (1) and the maximum (4) in the LICS profile of ionization P versus $\Gamma_d\tau_p$. The effect of the duration of the probe-laser pulse (with long dressing pulse) is clearly revealed. Steady-state values (2 and 3) are shown by the dashed lines. They approach the former for large $\Gamma_d\tau_p$.

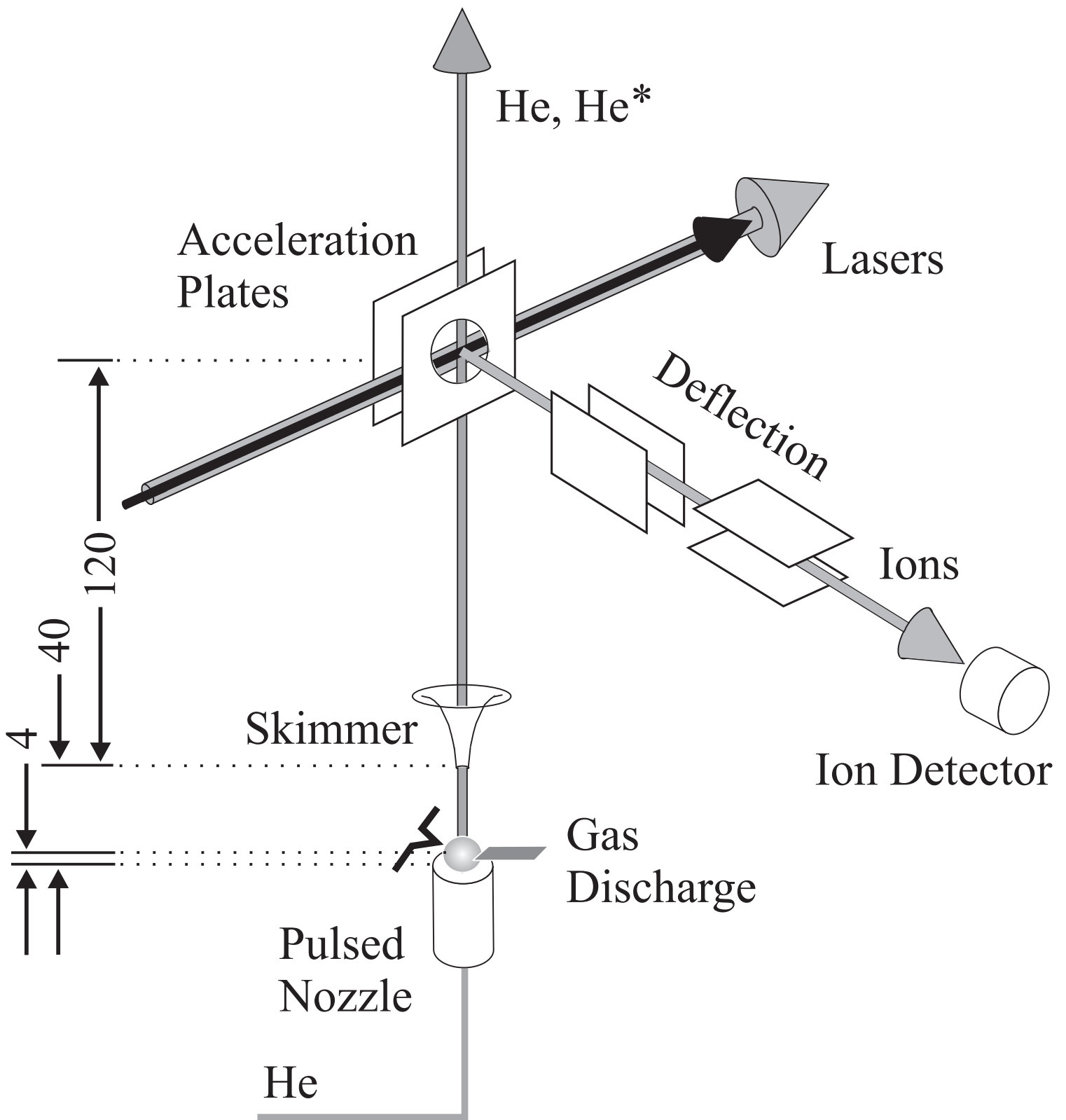
FIG. 15. Values of maximum (1) and minimum (2) in the LICS profile of ionization P versus $\Gamma_d\tau_p$ showing effect of pulse duration of probe pulse.

FIG. 16. LICS profile in various approximations. The solid line shows the result obtained by numerically solving Eqn. (12). The dashed line is the finite-bandwidth theory, Eqn (35). The dotted line is the quasistationary theory, Eqn (44). Here the dressing laser intensity is $I_d^{(0)} = 38 \text{ MW/cm}^2$, the probe laser intensity is $I_p^{(0)} = 2.5 \text{ MW/cm}^2$, $q = 0.73$, $\tau_p = 2.3 \text{ ns}$, $\tau_d = 5.1 \text{ ns}$, the laser pulses are coincident.

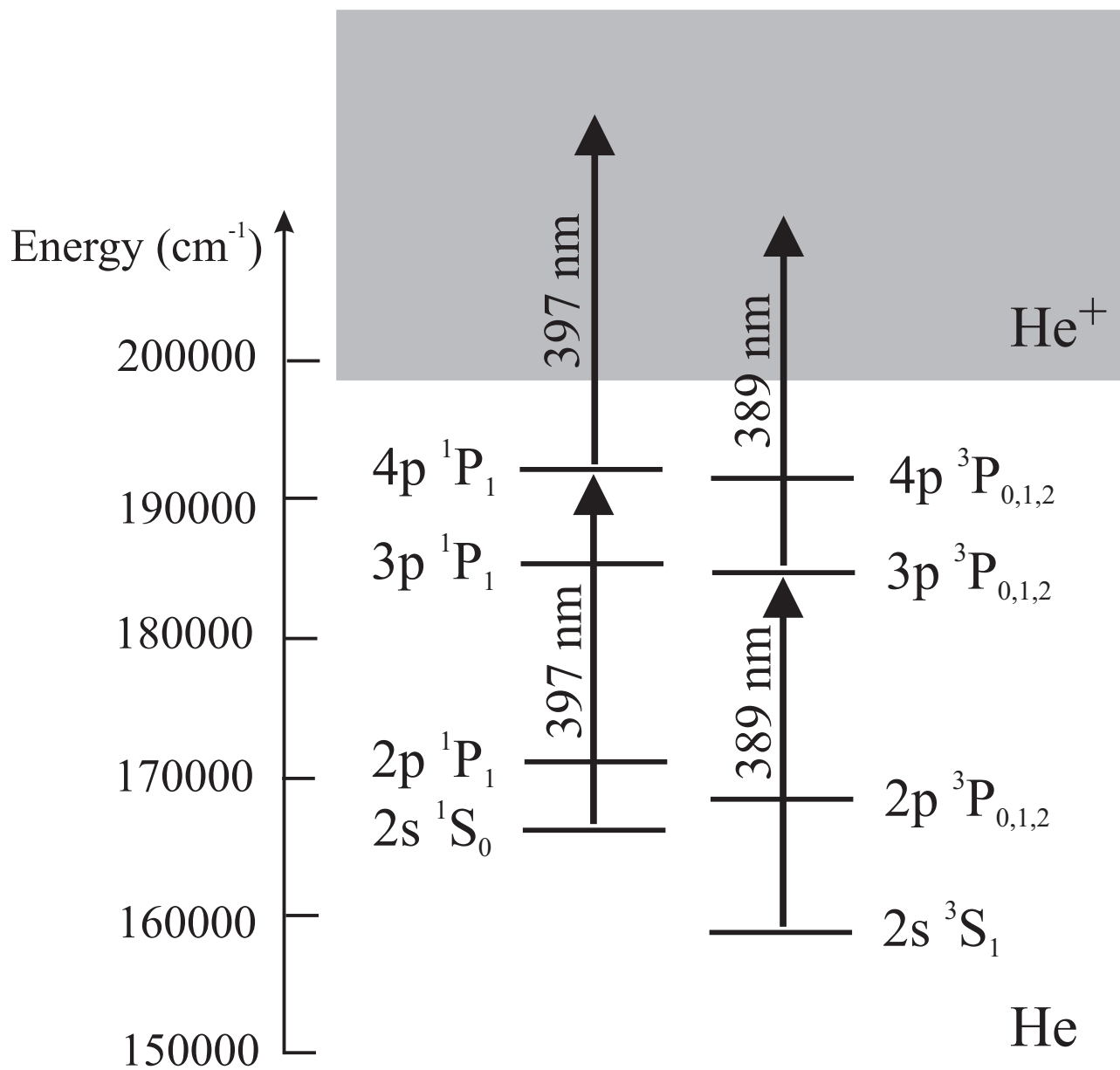
FIG. 17. Photoionization cross sections for the 2^1S state of He: 1 - this work, 2 - [75], 3 - [76], 4 - [77] ($1\text{Mb}=10^{-18} \text{ cm}^2$).



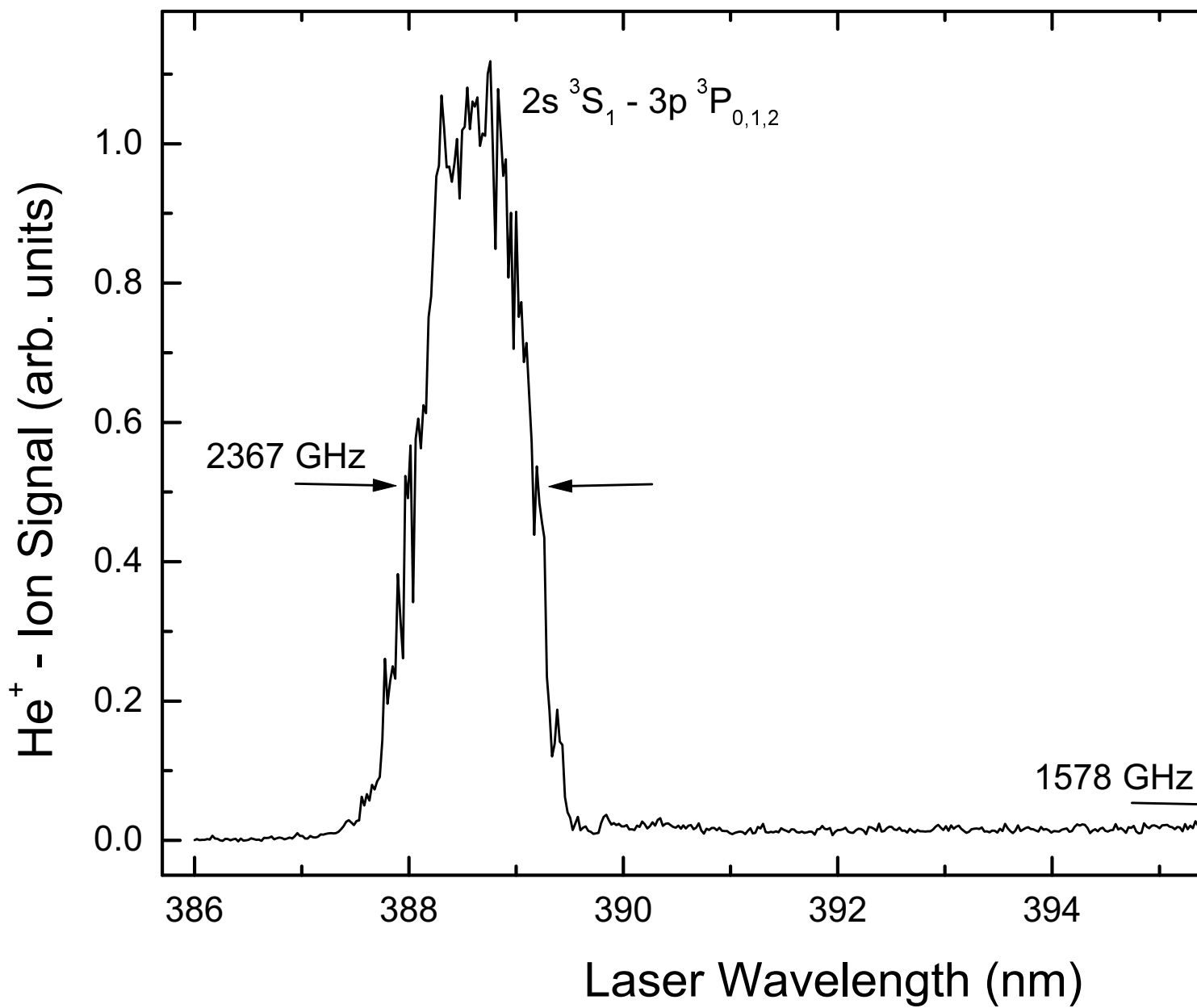
L.P. Yatsenko et al. , "Photoionization suppression by continuum coherence..." , Fig. 1

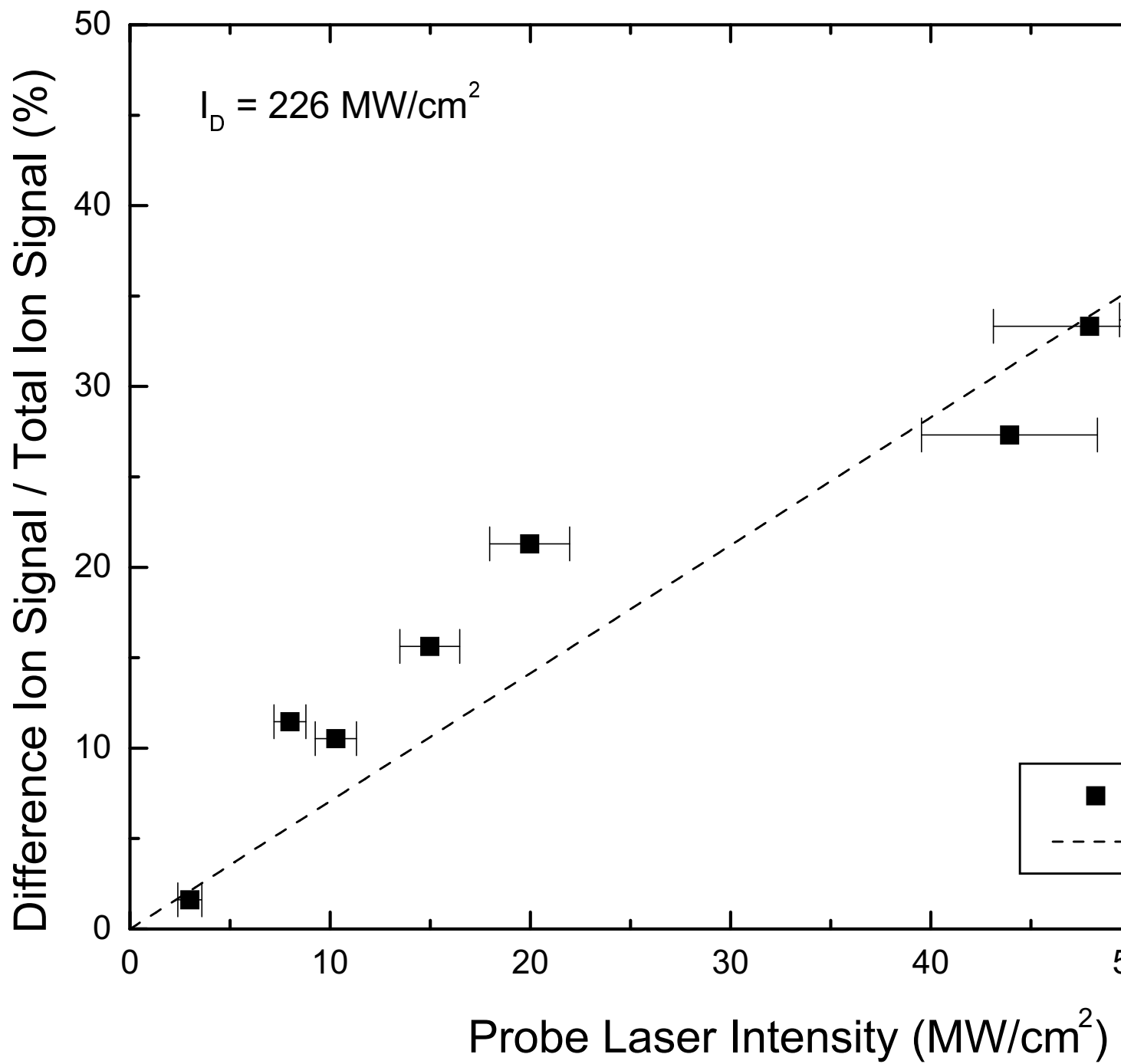


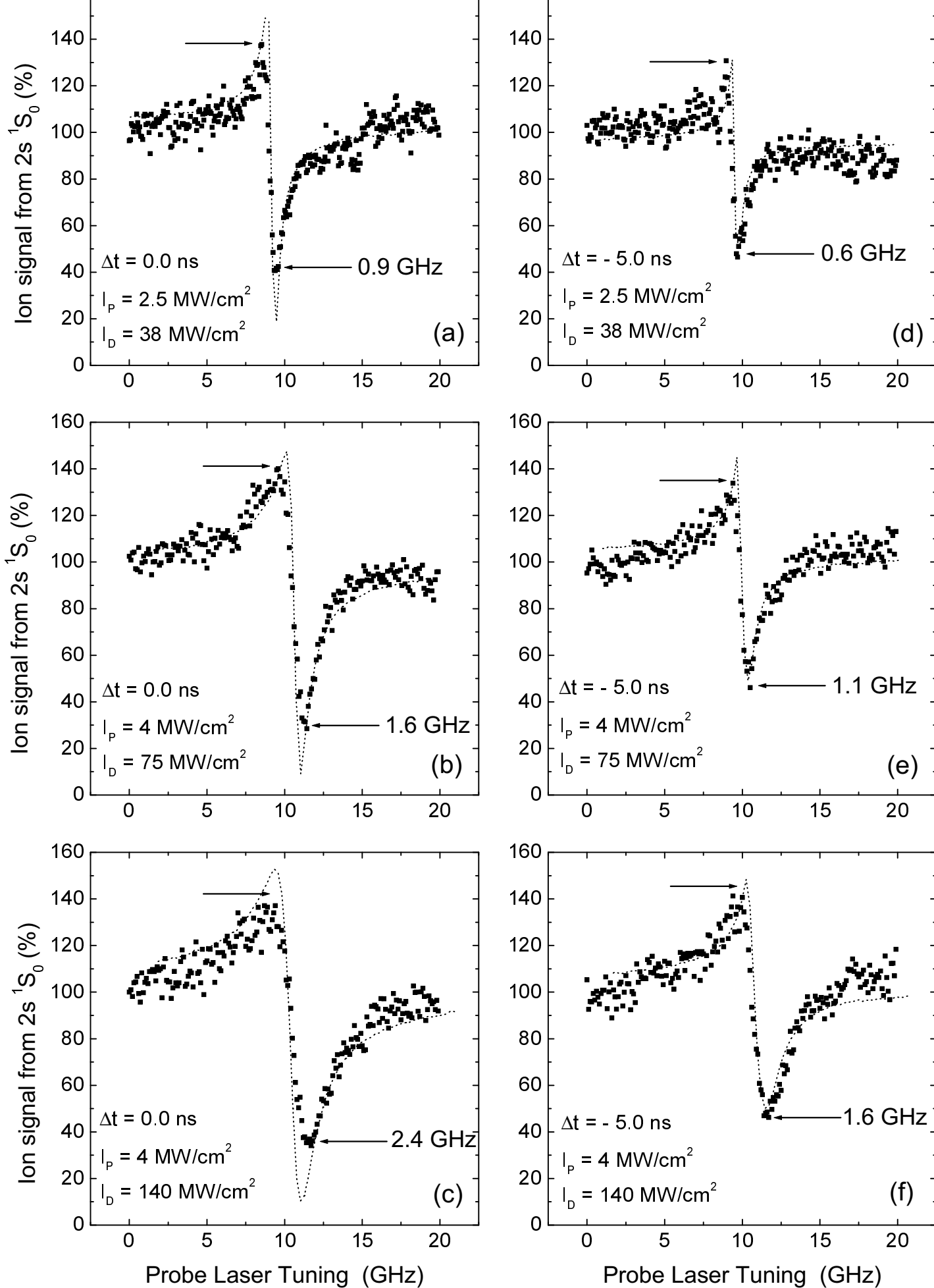
L.P. Yatsenko et al. , "Photoionization suppression by continuum coherence..." , Fig. 2

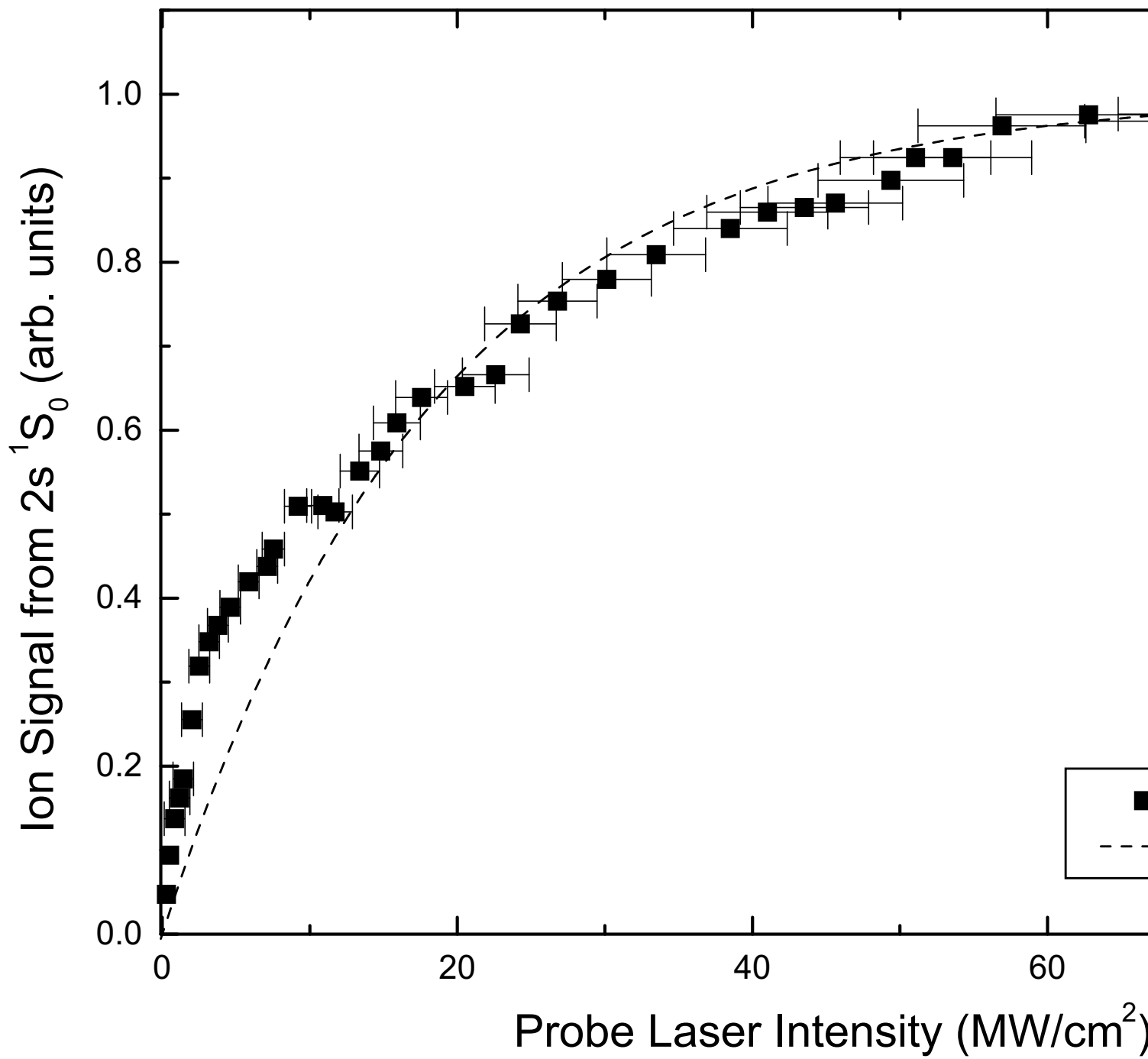


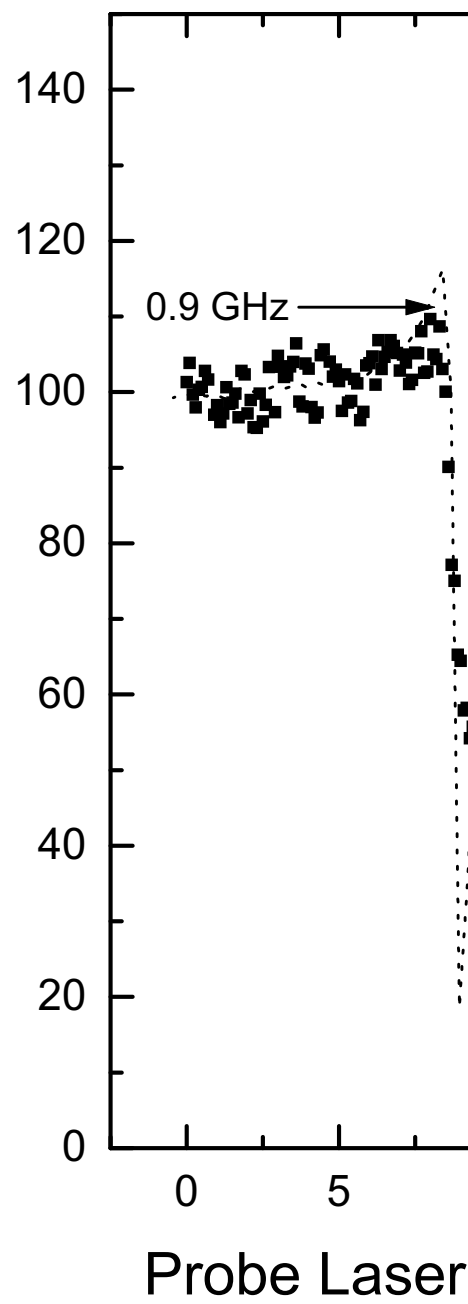
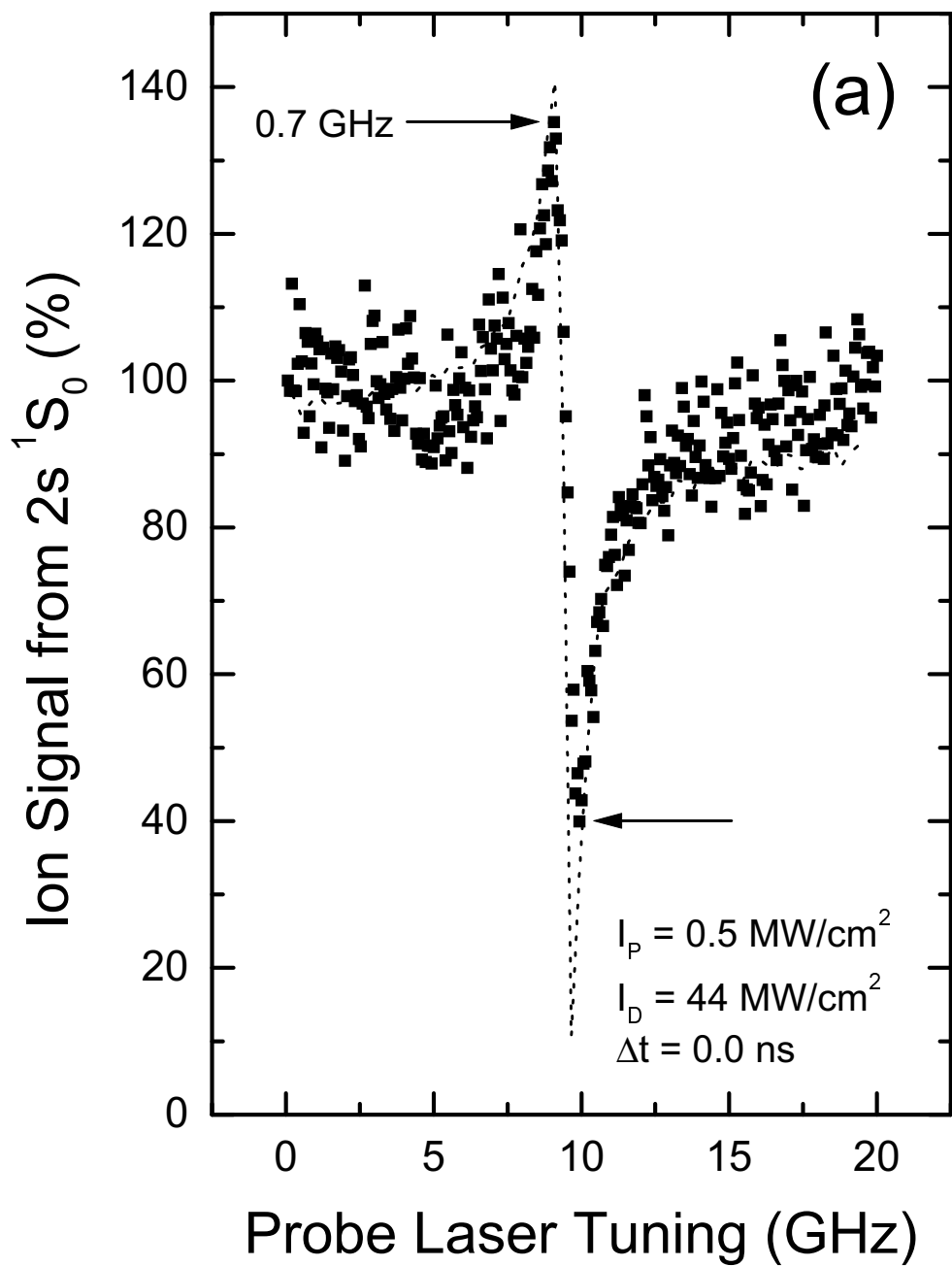
L.P. Yatsenko et al. , "Photoionization suppression by continuum coherence..." , Fig. 3

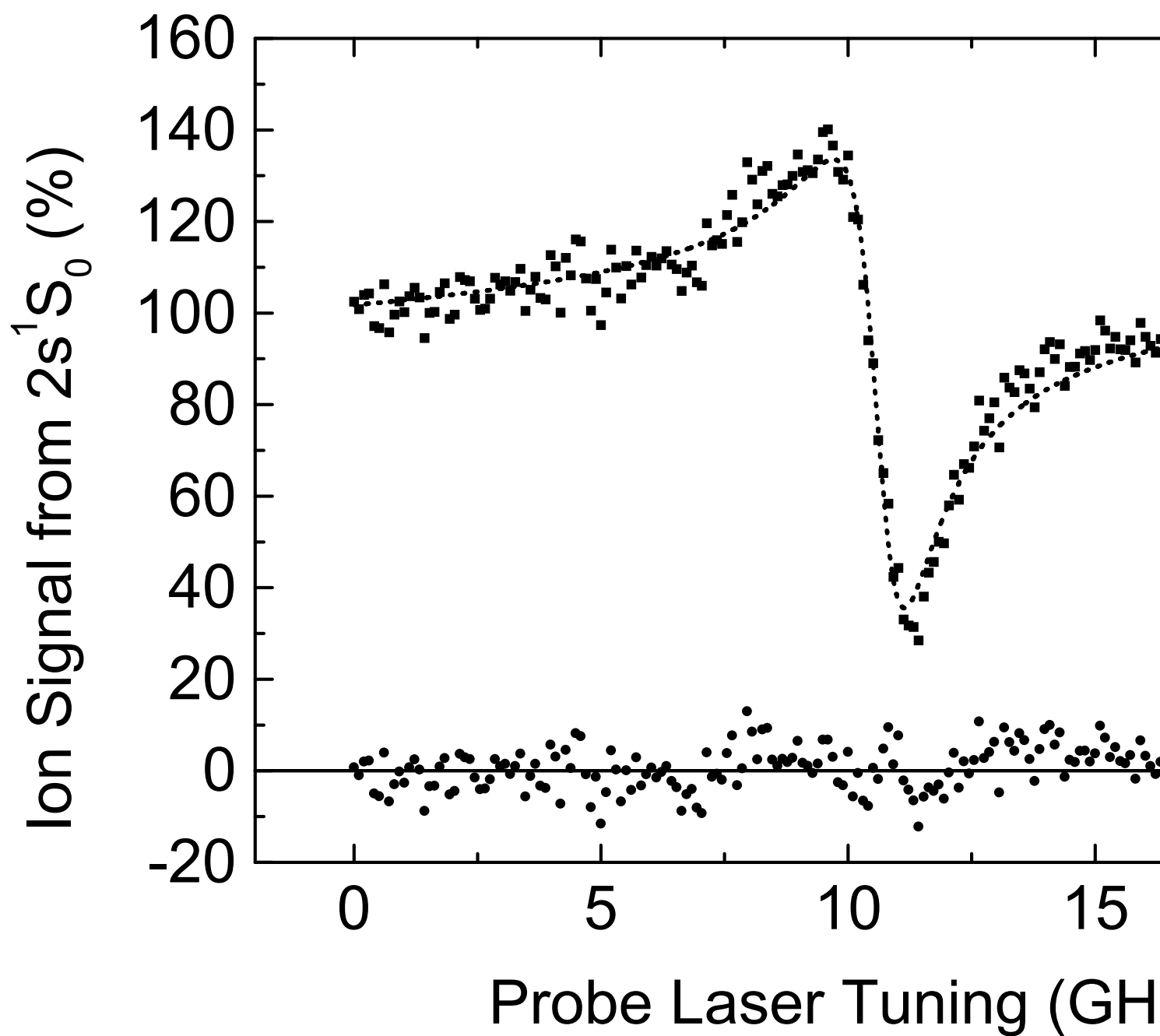


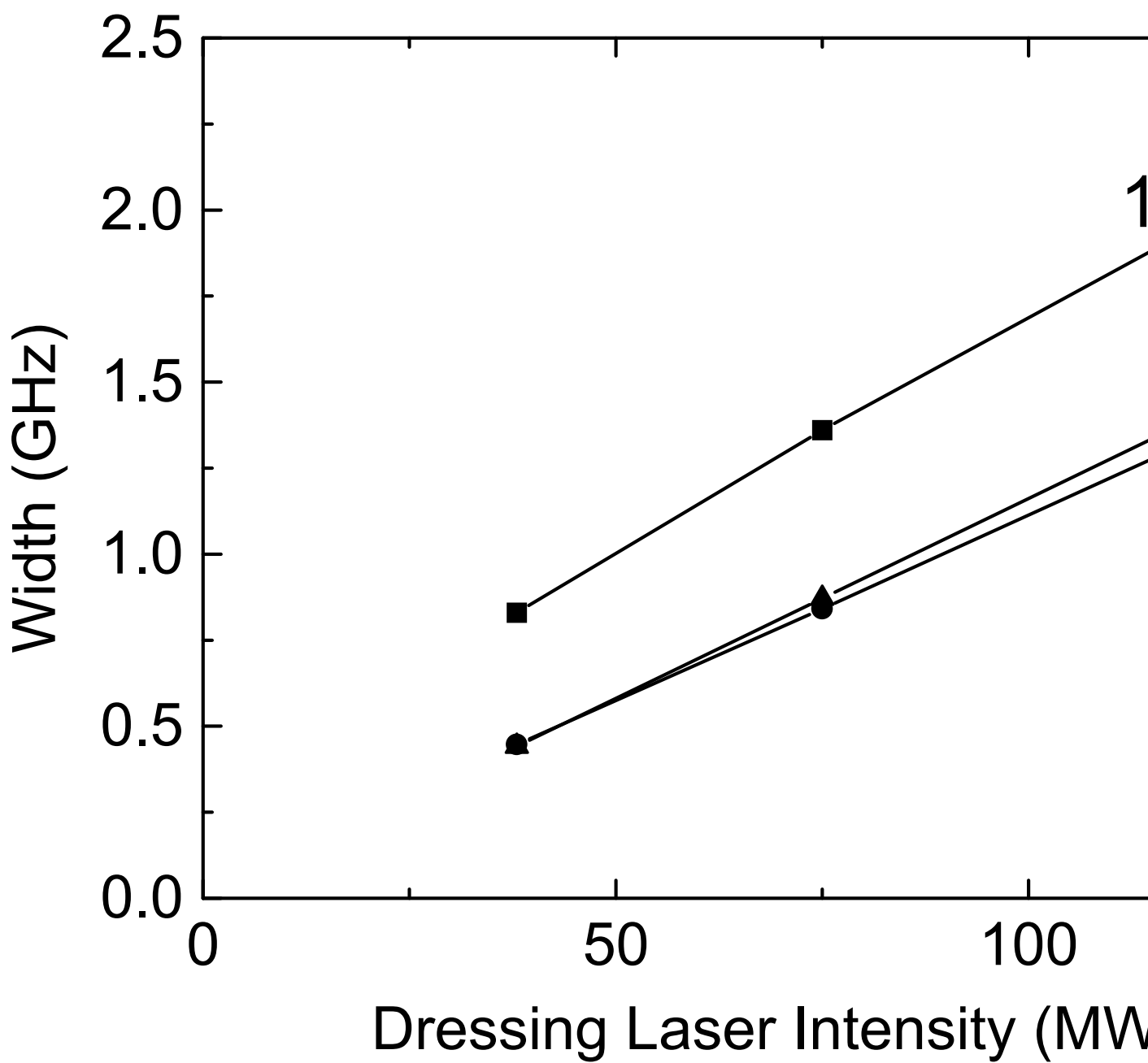


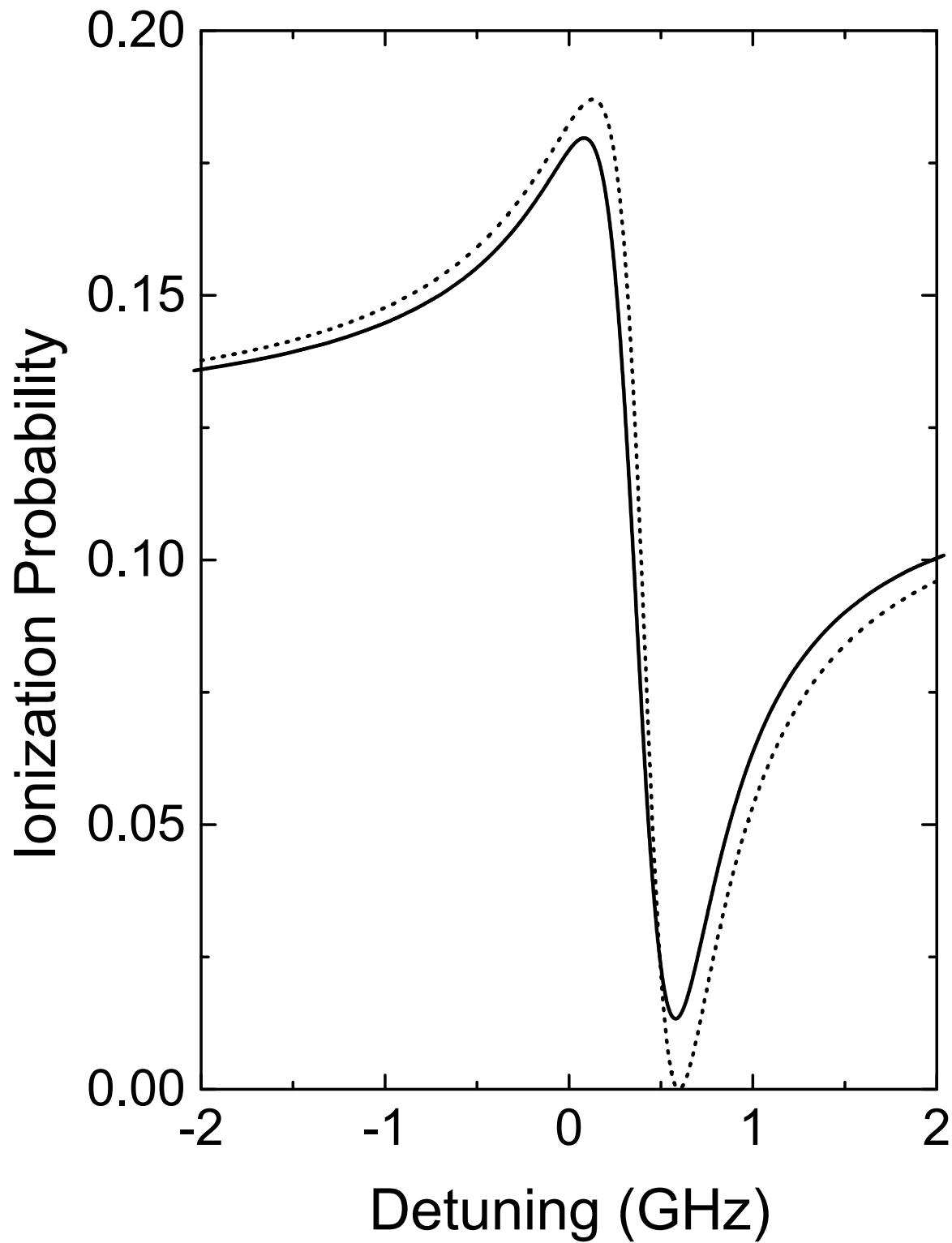


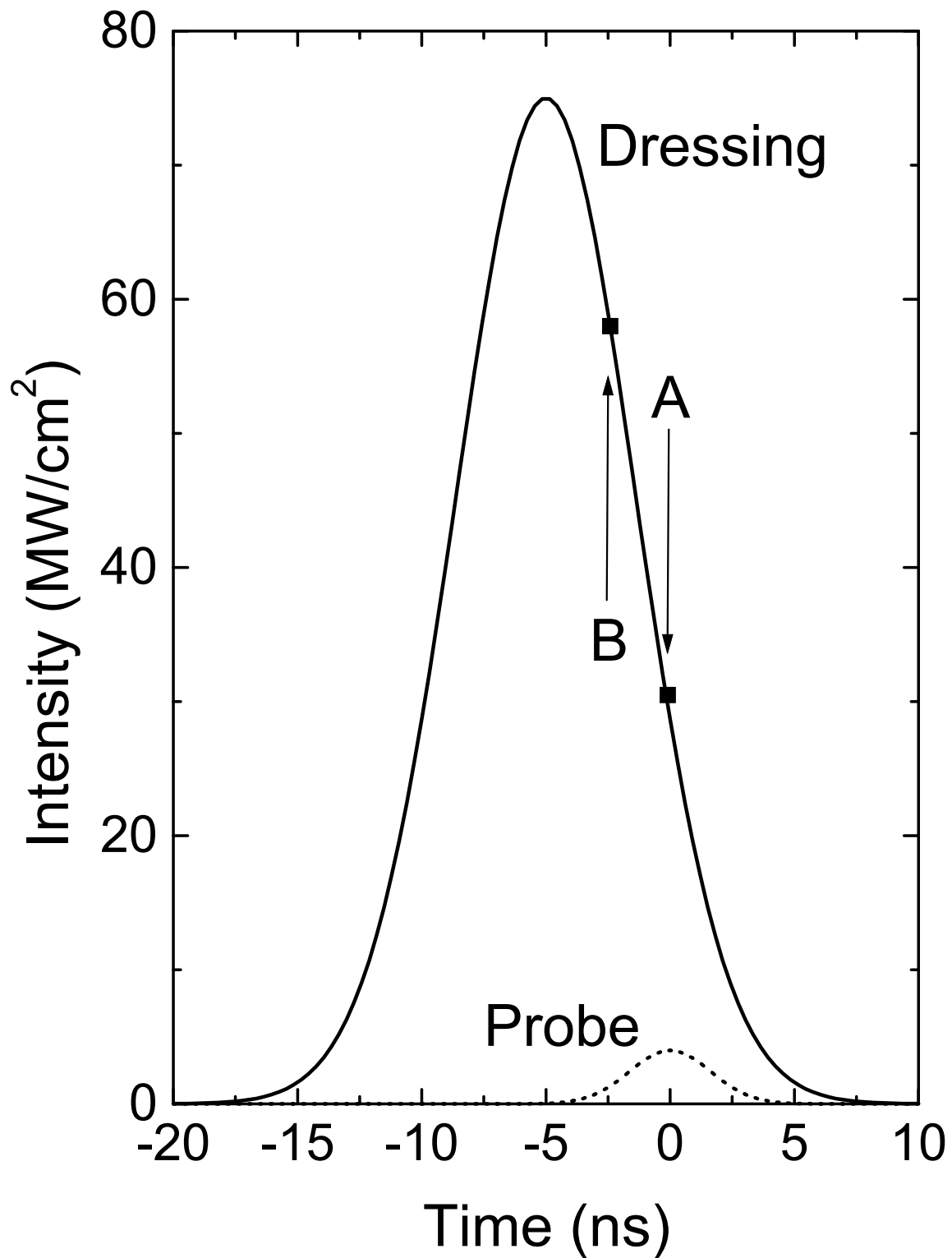




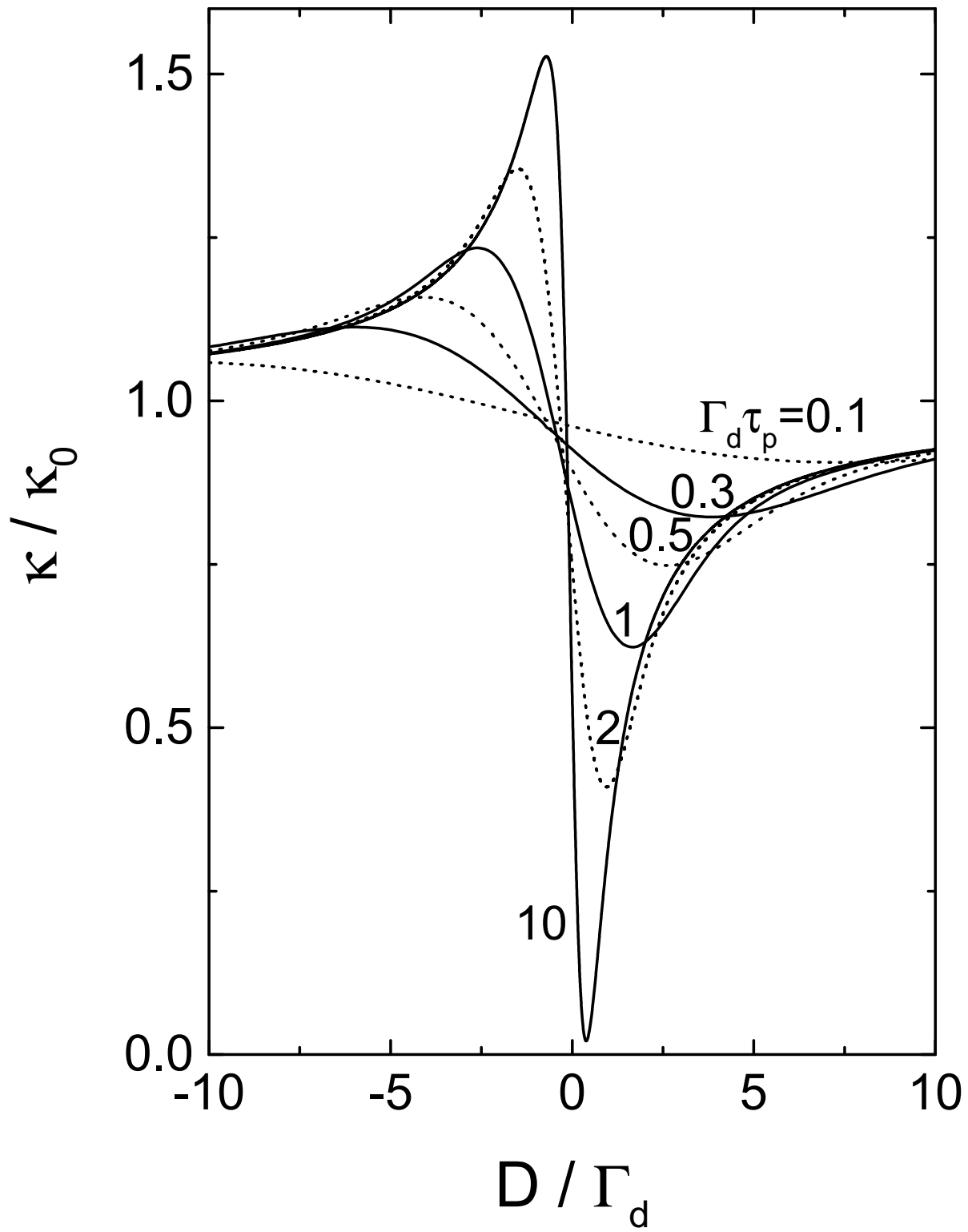




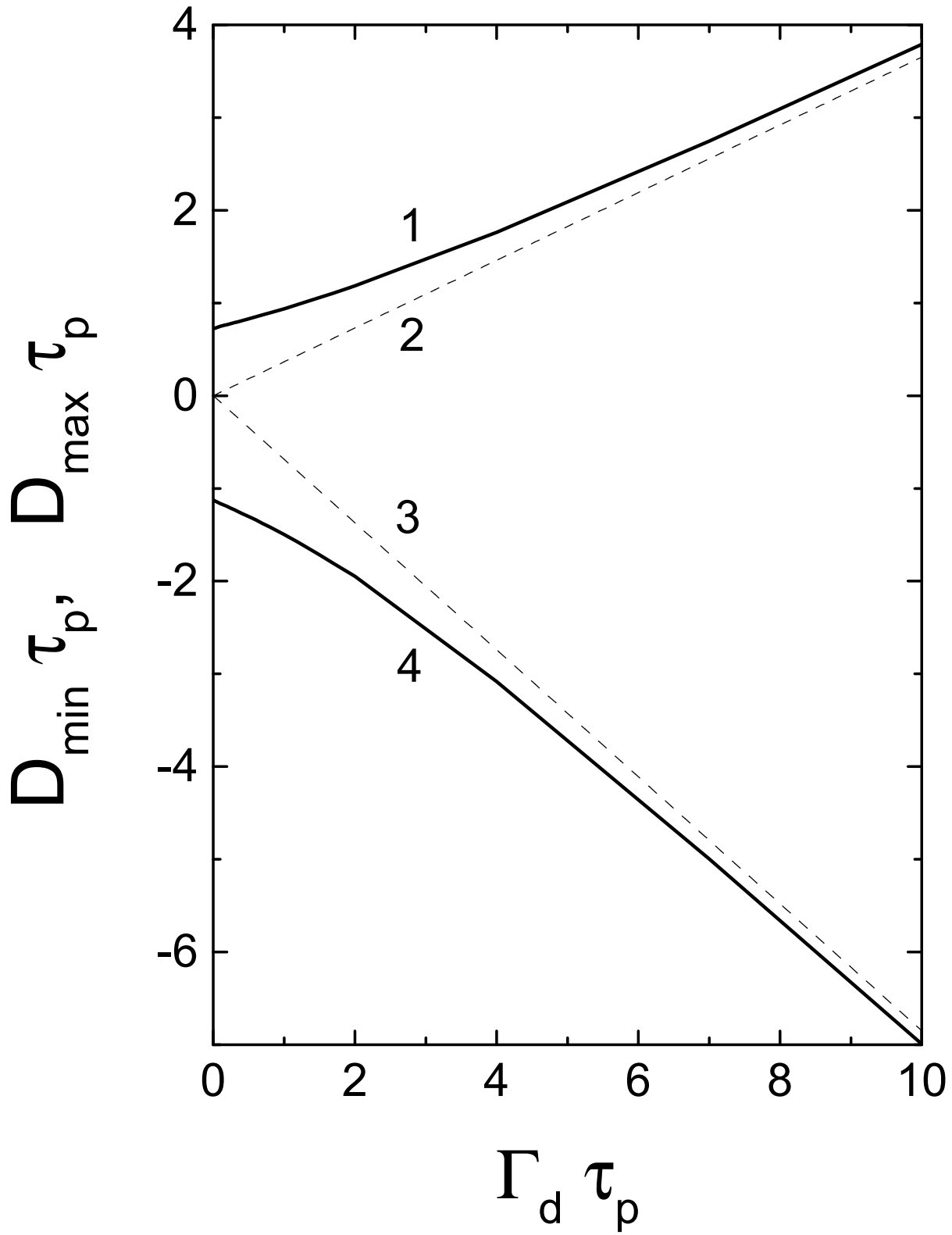




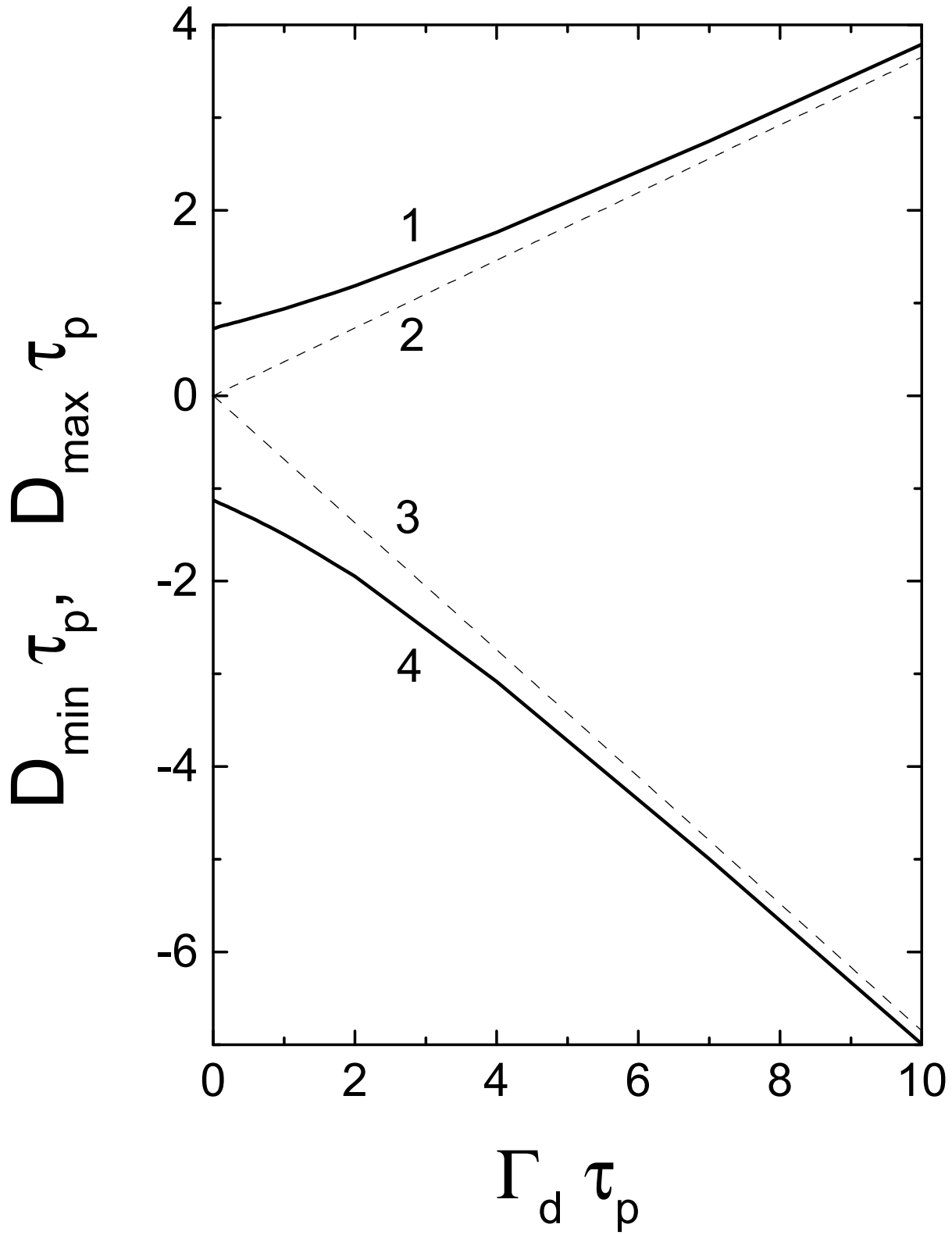
L.P. Yatsenko et al. , "Photoionization suppression by continuum coherence...", Fig. 12



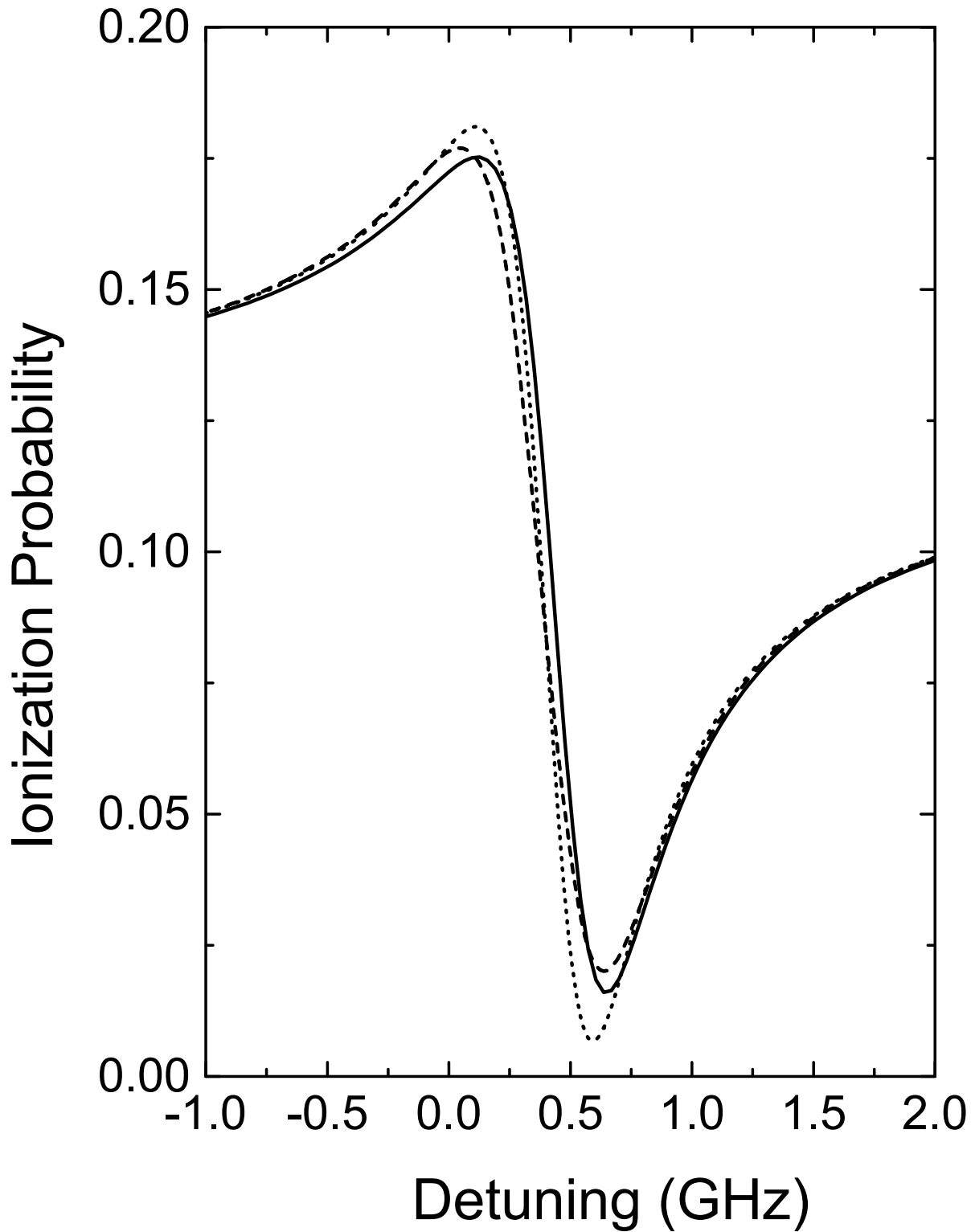
L.P. Yatsenko et al. , "Photoionization suppression by continuum coherence...", Fig. 13



L.P. Yatsenko et al. , "Photoionization suppression by continuum coherence...", Fig. 14



L.P. Yatsenko et al. , "Photoionization suppression by continuum coherence...", Fig. 14



L.P. Yatsenko et al. , "Photoionization suppression by continuum coherence...", Fig. 16

